NUMERICAL SIMULATIONS OF THE HVAB ROTOR IN HOVER

A Dissertation
Presented to
The Academic Faculty

By

Hajar Mali

In Partial Fulfillment
of the Requirements for the Degree
Master of Science in the
Daniel Guggenheim School of Aerospace Engineering

Georgia Institute of Technology

December 2022

NUMERICAL SIMULATIONS OF THE HVAB ROTOR IN HOVER

Thesis committee:

Dr. Lakshmi Sankar
Department of Aerospace Engineering
Georgia Institute of Technology

Dr. J.V.R. Prasad
Department of Aerospace Engineering
Georgia Institute of Technology

Dr. Stephen Ruffin
Department of Aerospace Engineering
Georgia Institute of Technology

Date approved: October 31, 2022

ACKNOWLEDGMENTS

I would like to seize this opportunity to thank my advisor Dr. Lakshmi Sankar for trusting me with this project, his guidance, and all the knowledge he passed on to me throughout this research. My thanks are extended to Dr. Stephen Ruffin and Dr. J.V.R. Prasad for their support and their constructive feedback and insights. I want to thank the faculty and administrative members at the Department of Aerospace Engineering at the Georgia Institute of Technology and at my home university, International University of Rabat, for the amazing program that has allowed me to study in three different continents.

I am also grateful to my friends at the CFD laboratory, Aishwerya S.G. and Shivani S., for their support. I am appreciative of my friends Wiame B. and Youssef L. as well for their belief in me. Lastly, I would like to express my profound gratitude to my parents for continuously pushing me to improve and follow my dreams.

TABLE OF CONTENTS

LIST OF TABLES

LIST OF FIGURES

NOMENCLATURE

T	=	thrust
Q	=	torque
P	=	power
C_T	=	thrust coefficient
C_Q	=	torque coefficient
C_P	=	power coefficient
FM	=	figure of merit
C_p	=	pressure coefficient
σ	=	solidity
Ω	=	angular velocity
ρ	=	density
A	=	swept area by the rotor
R	=	rotor radius
c	=	chord length
k	=	turbulent kinetic energy
ω	=	specific turbulent dissipation rate
μ_t	=	turbulent viscosity
μ	=	viscosity
t	=	time
ϵ	=	turbulence dissipation rate
γ	=	intermittency
$Re_{\theta,t}$	=	transition onset criteria
λ_i	=	induced velocity coefficient
κ	=	non-uniform flow and tip loss factor
$C_{P_{induced}}$	=	induced power coefficient

SUMMARY

Numerical simulations of compressible viscous flow over the Hover Validation and Acoustic Baseline (HVAB) rotor in hover are presented. A commercial flow solver, ANSYS Fluent, has been employed. The effects of transition are modeled using the Langtry-Menter k-ω SST-γ-Re_θ model at three different pitch settings. Comparisons with HVAB test data and other publications are discussed. These include integrated thrust and power coefficients, figure of merit, velocity inflow, surface pressure distribution, lift distribution, transition locations, and vortex structures. The presented work is an improvement and continuation of a previous effort.

CHAPTER 1
INTRODUCTION

1.1 Background

Countless advancements and innovations have been carried out within the rotorcraft industry over the past decade. Many rotor configurations and blade planforms have been studied to evaluate and ensure the highest efficiency and performance of rotorcraft throughout different flight phases. Researchers have conducted numerous computational and experimental studies that have been eventually published and shared within the rotorcraft community. Different workshops and meetings are held on a yearly basis to promote collaboration and maximize the accuracy of the computational predictions for helicopter flight such as the American Institute of Aeronautics and Astronautics (AIAA) and the Vertical Flight Society (VFS). Some of these workshops have targeted research for the S-76 rotor with various tip configurations including taper, sweep and anhedral angles. The research endeavour has then shifted towards the Pressure Sensitive Paint (PSP) rotor tested at the National Aeronautics and Space Administration (NASA) Langley Research Center as well as the most recent rotor configuration: the Hover Validation and Acoustic Baseline (HVAB) rotor tested at the NASA Ames Research Center.

The PSP blade configuration was inspired from the High Lift Rotor (HLR) blade set created back in 2002, and resulted from a collaboration between the U.S. Aviation Development Directorate (ADD) and NASA. In 2007, the rotor blades were tested in the 14x22 Rotor Test Cell at NASA Langley to evaluate the accuracy of the Computational Fluid Dynamics (CFD) performance predictions. As for the HVAB blade set, it was developed in partnership with the NASA Revolutionary Vertical Lift Technology (RVLT) Project and the US Army Combat Capabilities Development Command Aviation Missile Center, and was

manufactured in 2020. Its specific blade geometry was highly inspired from the PSP blade planform with only minor discrepancies between the two, to name but a few, having different hubs and attachment points, different trailing edge thickness (0.0350" for the HVAB blade versus 0.0300" for the PSP blade), as well as a small dissimilarity in the root fairing shape.

1.2 Objectives

The HVAB rotor is the focus of the research conducted within this Master thesis. It is modeled using the Fluent solver to evaluate its hover performance at three different pitch settings and to compare the predictions with the HVAB test data. Induced power and velocity inflow are also investigated. Moreover, the tip vortex structure and the rotor inner wake are captured. The locations at which the flow transition occurs on the upper and lower surfaces of the HVAB blade are also identified within this work, along with the surface pressure and lift distributions at multiple radial blade sections.

1.3 Prior Research

Prior work was published within the AIAA SciTech Forum held in San Diego in January 2022. The study was conducted using the commercial solver ANSYS Fluent to model the HVAB rotor in hover condition at different pitch settings using three different turbulence models: Spalart Allmaras, k-ω, and Transition SST. In addition to the performance predictions, the effects of coning and lag angles inclusion on the rotor performance were investigated. The coning and lag angles implemented in the simulations were taken from the AIAA website and had little to no effect on the performance predictions. Coning angles were also re-computed at the end of the simulations and were lower compared to the provided AIAA values. The effect of transition modeling was also investigated and showed slight improvement in terms of overall rotor performance. [1]

Further investigation and refinement were deemed necessary to improve the performance predictions and to properly capture the transition over the blades and the vortex structures, namely the tip vortices that are an important attribute in the wake of helicopter rotors. The presented work is both an improvement and continuation of this previous effort.

1.4 Rotor Aerodynamics and Hover Condition

Unlike fixed wing aircraft, helicopter rotors operate in highly unsteady environments, hence the higher aerodynamic complexity. Different combinations of tip configurations have been analyzed to maximize the rotors efficiency and attenuate stalling. Starting from the 1970s, multiple helicopters such as the UH-60 Blackhawk and the AH-64 Apache included swept tips in their rotor configuration as it has been proven that a swept tip blade results in a reduced stalling behavior in contrast with a regular blade tip mainly due to the formation of a vortex structure around the leading edge. However, at high angles of attack, sweeping the tip might not necessarily enhance the performance as desired. In 1972, Sikorsky has been awarded the technological basis of the S-76 which incorporated different rotor blade aerodynamic characteristics such as twist, swept tips, and so on. Moreover, since the late 1990s, anhedral blade tips have been implemented to weaken and diffuse vortices.

Helicopter rotors can contain multiple blades, and each blade can be composed of different airfoil types. Helicopters in general can perform several maneuvers unlike ordinary aircraft. It can land and take off vertically and it also can remain in one fixed position in the air which is referred to as hover. The main challenge during hovering is balancing the loads and moments. The helicopter descends when the produced lift by the main rotor is not enough to balance its weight, and gains height if the lift generated is higher. To hover, the pilot changes the orientation of the blades to a specific pitch angle. Pitch angle refers to the angle between the chord line and the reference plane in which the rotor hub lies. Implementing a pitch increase to the rotor blades is done via the Collective Control. Raising

the Collective moves the Swashplate which is then responsible for transmitting the motion through the main rotor drive shaft and rotating all of the blades to a specific pitch setting simultaneously. Yaw control can also be ensured through the use of two rotors with opposite rotational directions or by tilting the helicopter rotor disk left and right.

The source of a hovering helicopter's drag is mostly induced drag resulting from the lift generation which consequently increases the total power required. In addition, the blades experience some profile drag due to their rotational motion in the air. The generated tip vortices of the preceding blades have a significant impact on the lift production of the following ones. These vortex-blade interactions lead to an increase in power requirement during hover.

Another important phenomenon related to hovering is the in ground effect which usually takes place at an altitude that does not exceed one rotor diameter above the surface. When hovering within that range of altitude, lift increases as the induced flow is decreased due to the obstruction of the ground surface. Consequently, the angle of attack increases and less power is required for the production of the desired lift amount. In contrast, if it hovers at a higher altitude then it is hovering out of ground effect. With no induced flow reduction, the angle of attack and the generated lift decrease. In this case, sustaining the same angle of attack requires an increase in pitch which also contributes to drag and decelerates the rotational speed of the blades. Thus, the engine power has to be raised to preserve the same rpm.

CHAPTER 2

HVAB ROTOR DESCRIPTION

The HVAB rotor is a helicopter rotor with four blades operating at a speed of 1250.39 rpm. To model this rotor in ANSYS Fluent, the domain periodicity is taken advantage of for the reduction of computational time by conducting simulations on a single blade then projecting the calculations onto the entire rotor disk. The HVAB blade is 1.6891 m (66.5in) long and is made of three RC-series rotorcraft airfoils: RC(4)-12, RC(4)-10, and RC(6)-08 with a decreasing thickness from root to tip. The rotor operates at a tip Mach number equal to 0.65. The HVAB blade planform is shown in Figure 2.1.

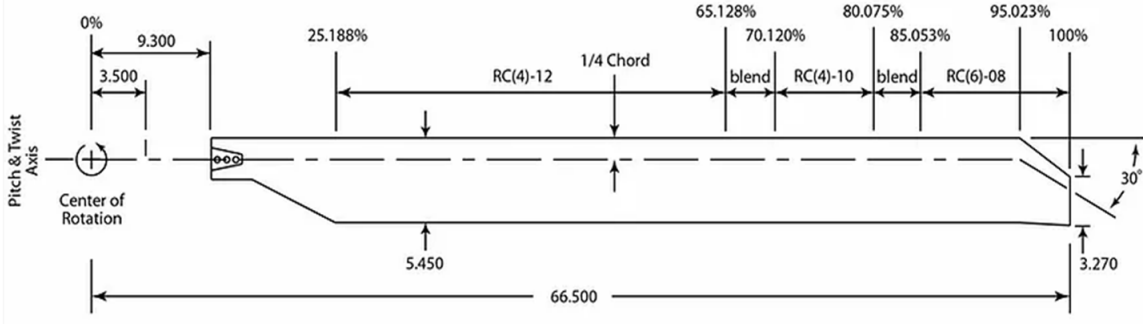

Figure 2.1: HVAB rotor blade geometry from: https://www.aiaa-hpw.org/hvab-rotor.

Table 2.1: HVAB rotor operating conditions.

Parameters	Value
Number of blades	4
Radius (in)	66.5
Solidity	0.1033
Reference chord (in)	5.45
Tip chord (in)	3.27
Tip Sweep at 95%R	30°
Flap hinge (in)	3.5
Rotor Speed (rpm)	1250.39
Tip Mach Number	0.65

The HVAB rotor blades are twisted linearly at an angle of 14 degrees from root to tip (see Figure 2.2) [2] in order to reduce internal blade stress and also to allow a more even distribution of lift along the blade since the variation of the relative wind leads to lift differential. Higher twist angles are implemented at the root since that region experiences lower velocities, and lower twist angles are used closer to the tip where the velocities are higher.

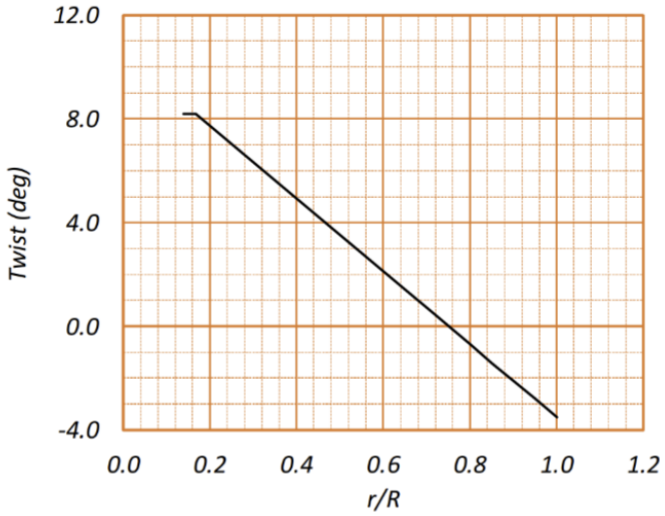

Figure 2.2: HVAB rotor blade spanwise twist variation.[2]

CHAPTER 3
METHODOLOGY

3.1 Software and Numerical Approach

Relying solely on experimentation can be extremely costly, time-consuming and might require heavy alterations to the setup. Therefore, conducting numerical studies can save both money and time and also allow more flexibility and ease of implementation of modifications to the geometry, flow conditions and so on with no major waste of resources. The accuracy of numerical findings can be validated through the experimental data collected. Thanks to these CFD tools, it became possible to achieve an efficient use of resources while thoroughly analyzing the influence of tip planforms on rotor performance or vortex-blade interactions under different flight phases and conditions. The impact of the CFD tools can extend beyond aerodynamics to include aeroacoustics. For instance, the proper identification of pressure distribution is quite useful in terms of loading noise and thickness noise computations.

This work is conducted using the CFD commercial software ANSYS. The simulations are ran using the Fluent solver which provides a large selection of turbulence and transition models. A variety of grid generation and post-processing tools are made available to the user as well. ANSYS can be used for modeling steady and unsteady, 2-D and 3-D flows, and also ensures both the ease of accessibility and manipulation due to its intuitive user-friendly interface. The version 2021R2 of ANSYS is employed under research license. Knowing that the total grid cell count is around 15 million cells, the running time for each simulation was around 72 hours with the use of 6 solver processes on a desktop used with 6 cores and 12 logical processors.

3.2 Transition Modeling

The turbulence model employed to include transition effects within this work is the four-equation k-ω SST-γ-Re_θ model. It couples the two equations of the k-ω fully turbulent model with two additional equations introducing intermittency and transition onset criteria. Understanding the mathematics behind the this model requires a first discussion of the two-equation k-ω model and then extending it to the four equation k-ω SST-γ-Re_θ model.

3.2.1 k-ω fully turbulent model

k-ω model is a very common model used for capturing the effect of turbulent flow conditions. In comparison to the other popular turbulence model k-ϵ, k-ω is better suited for aerodynamics applications since it provides much higher accuracy for boundary layer predictions in the presence of adverse pressure gradients. k represents the turbulent kinetic energy while ω refers to the specific turbulent dissipation rate (1/s). k and ω are described by the following transport equations:

$$\frac{\partial(\rho\, k)}{\partial t} + \nabla.(\rho U k) = \nabla.((\mu + \frac{\mu_t}{\sigma_k})\nabla k) + P_k - \rho\epsilon \tag{3.1}$$

$$\frac{\partial(\rho\, \omega)}{\partial t} + \nabla.(\rho U \omega) = \nabla.((\mu + \frac{\mu_t}{\sigma_k})\nabla \omega) + \frac{\gamma}{\nu_t} P_k - \beta\rho\omega^2 \tag{3.2}$$

μ_t is the turbulent viscosity and σ_k, β, and γ are empirical coefficient.

ϵ is the turbulence dissipation rate (m^2/s^3). ω and ϵ are both linked such that:

$$\omega = \frac{\epsilon}{C_\mu k} \tag{3.3}$$

with:

$$C_\mu = 0.09 \tag{3.4}$$

3.2.2 k-ω SST-γ-Re_θ model

ANSYS Fluent provides a variety of models allowing transition to be taken into account. The present results have been generated for a transitional flow, using the four-equation k-ω SST-γ-Re_θ model. It is based on the coupling of the k and ω shear stress transport equations with two other transport equations- one corresponding to the intermittency and one to the transition onset criteria.

The k-ω SST-γ-Re_θ model is employed when trying to model turbulent flows in which a significant part of the boundary layer is laminar. It is best suited for external flows with important separation. This model couples the two transport equations of the k-ω SST model with two extra equations. Therefore, it solves for four different variables: k, ω, γ and $Re_{\theta,t}$. For this model, the first equation corresponding to k remains the same as the one of $k-\omega$ model.

The challenge arising from using k$-\omega$ is that it is highly dependent on the freestream turbulence conditions as was discussed by Menter [3]. For instance, small changes to the value of k_∞ would entail large changes in turbulent viscosity and in skin friction coefficient. This behavior would significantly influence the forces and flow separation. To overcome that, this model can switch from k-ϵ model to k-ω model and vice versa through the implementation of the blending function F_1 (see equation 3.5). When F_1 is 0, then the model adopted is k-ϵ (away from the wall) since unlike $k-\omega$, it is not dependent on freestream values. Conversely, when the blending function takes a value of 1, the model used is the k-ω model (near the wall). Equation 3.5 is the dissipation equation for the Langtry Menter k-ω SST-γ-Re_θ model and it is simply the same equation for $k-\epsilon$ model but with the last

term multiplied by $(1 - F_1)$ to allow the switch between k-ω and k-ϵ.

$$\frac{\partial(\rho\,\omega)}{\partial t} + \nabla.(\rho U\omega) = \nabla.((\mu + \frac{\mu_t}{\sigma_k})\nabla\omega) + \frac{\gamma}{\nu_t}P_k - \beta\rho\omega^2 + 2(1-F_1)\frac{\rho\sigma w^2}{w}\nabla k : \nabla\omega \quad (3.5)$$

The production of turbulent kinetic energy term P_k is multiplied by γ known as the turbulent intermittency such that if γ happens to be 0 then the flow is locally laminar and if it is equal to 1 then the flow is fully turbulent. And finally a transitional boundary layer is indicated by a value of γ between zero and one.

$$P_k \longrightarrow P_k\gamma \qquad 0 \leq \gamma \leq 1$$

A viscosity limiter is also implemented in the Transition SST model using the blending function F_2 (see equation 3.6). If S (magnitude of shear strain) or F_2 gets large then the viscosity is reduced. This second blending function is bigger when the distance to the wall is small.

$$\mu_t = \frac{a_1\rho k}{max(a_1\omega, SF_2)} \quad (3.6)$$

Since we are aware that the k-ω model performs better near the wall, it is desired to prevent the value of F_1 in the laminar boundary layer from switching from one to zero. Thus, the following modification is made:

$$F_{1,new} = max(F_1, F_3) \quad (3.7)$$

with:

$$F_3 = e^{-(\frac{R_y}{120})^3} \tag{3.8}$$

$$R_y = \frac{\rho y \sqrt{k}}{\mu} \tag{3.9}$$

In this manner, when the γ value is small, we are close to the wall and F_3 tends to one (k-ω used). In contrast, when the γ value is big, we are away from the wall and F_3 tends to zero (k-ϵ used).

$$\frac{\partial(\rho\gamma)}{\partial t} + \frac{\partial(\rho U_j \gamma)}{\partial x_j} = P_{\gamma 1} - E_{\gamma 1} + P_{\gamma 2} - E_{\gamma 2} + \frac{\partial[(\mu + \frac{\mu_t}{\sigma_\gamma})\frac{\partial \gamma}{\partial x_j}]}{\partial x_j} \tag{3.10}$$

In the third transport equation solving for γ, the transition sources responsible for controlling the length of the transition region are defined by the following production and dissipation terms:

$$P_{\gamma 1} = C_{a1} F_{length} \rho S [\gamma F_{onset}]^{C_{\gamma 3}} \tag{3.11}$$

$$E_{\gamma 1} = C_{e1} P_{\gamma 1} \gamma \tag{3.12}$$

where F_{Length} controls the production strength and F_{Onset} switches on production of intermittency. The stronger the production is, the faster γ saturates to 1 and the shorter the transition region is. F_{Length} and F_{Onset} are controlled by additional empirical functions.The remaining terms $P_{\gamma 2}$ and $E_{\gamma 2}$ are known as the destruction/relaminarization terms.

The fourth shear stress transport equation is:

$$\frac{\partial(\rho \hat{Re}_{\theta t})}{\partial t} + \frac{\partial(\rho U_j \hat{Re}_{\theta t})}{\partial x_j} = P_{\theta t} + \frac{[\sigma_{\theta t}(\mu + \mu_t)\frac{\partial \hat{Re}_{\theta t}}{\partial x_j}]}{\partial x_j} \tag{3.13}$$

An important term related to the last equation is $Re_{\theta,t}$ which is the single fixed value

referring to the Reynolds number where transition occurs. To predict the transition location, $\hat{Re}_{\theta,t}$ is computed everywhere in the flow and is forced to freestream value $Re_{\theta,t}$ by the source term $P_{\theta,t}$.

3.3 Performance Assessment

In this work, the performance of the HVAB rotor is evaluated in hover condition. Three performance indicators are utilized: the thrust coefficient, power coefficient, and figure of merit. The latter characterizes the efficiency of the rotor which corresponds to the ratio of the ideal power to the actual power.

$$C_T = \frac{T}{\rho A(\Omega R)^2} \tag{3.14}$$

$$C_Q = \frac{Q}{\rho AR(\Omega R)^2} \tag{3.15}$$

$$C_P = \frac{P}{\rho A(\Omega R)^3} \tag{3.16}$$

$$FM = \frac{C_T\sqrt{\frac{C_T}{2}}}{C_Q} \tag{3.17}$$

where:

-T is thrust.

-Q is torque.

-ρ is density.

-Ω is the angular velocity which is equal to 1250 rpm that is 130.94 rad/s.

-R is the rotor radius.

-A is the swept area by the rotor that is calculated in the following manner:

$$A = \pi R^2 = 8.963m^2 \tag{3.18}$$

In hover condition, the power is equal to the product of angular velocity and torque:

$$P = \Omega Q \tag{3.19}$$

Therefore, in the hover case, the power and torque coefficients are equal:

$$C_P = C_Q \tag{3.20}$$

After the convergence of the simulations, thrust and torque values are extracted. The coefficients of thrust and power are then calculated and plotted against the results from the previous work [1] as well as the test data of the HVAB rotor in hover condition [4].

CHAPTER 4
GRID GENERATION

In prior work, an unstructured grid made of around 2.4 million tetrahedral and hexahedral cells was generated for the fluid domain where the flow field was divided into four regions; one region per blade. This fluid enclosure had a shape of a quarter of a cylinder with two periodic boundaries corresponding to the two lateral sides that transfer data onto the full rotor disk. The inlet was located at a distance equal to 3 rotor radii above the blade and the outlet at 6 rotor radii beneath it. A sphere of influence of radius 10 times the chord length (1.4 m radius) was used for further refinement around the blade. The blade surface used a structured grid made of over 86000 triangular faces with a refined leading edge and tip regions.

The current work uses over 15 million mesh cells with 238630 triangular wall faces to improve the accuracy of the performance predictions and the quality of the generated contours. This refinement is implemented both on the blade surface and fluid domain. For the blade grid, the number of divisions chordwise is increased and the mesh size along the trailing edge is reduced. The domain is refined by reducing the global element size of the farfield and the element size of the sphere of influence around the blade.

Figure 4.1 displays the flow domain mesh and dimensions with a zoomed-in view of the further refinement corresponding to the sphere of influence created in the vicinity of the blade.

Wall Y+ is a non-dimensional distance measured from the wall. It defines how coarse or fine a mesh is for a specific flow analysis. Y+ < 1 is needed to ensure that the cells near the wall domain are of a proper size. To satisfy this condition, the first layer thickness had

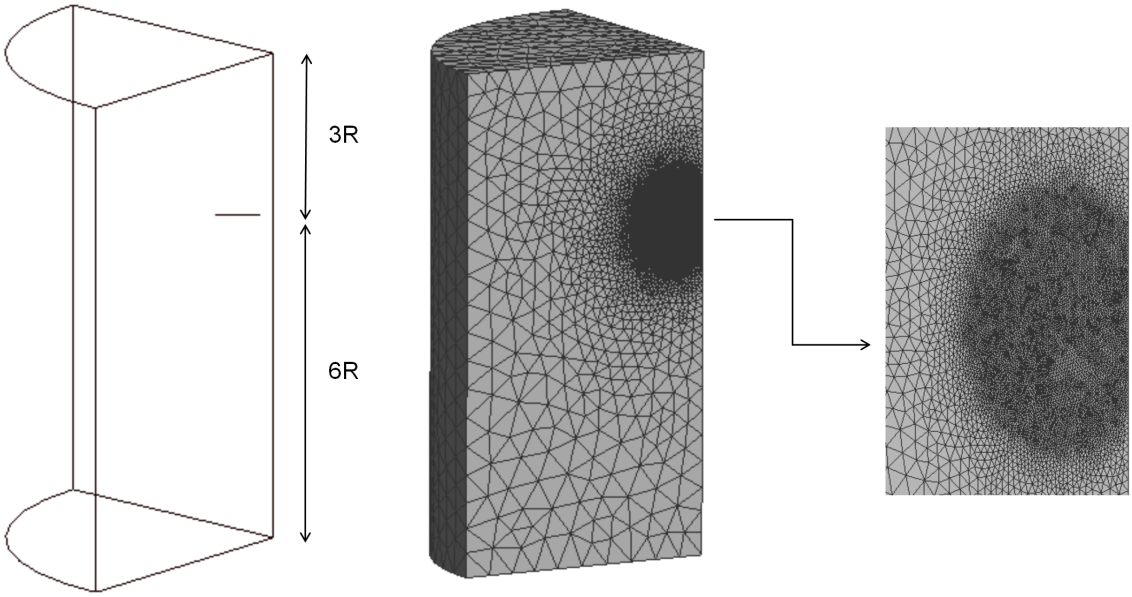

Figure 4.1: Generated outer grid with sphere of influence around the blade.

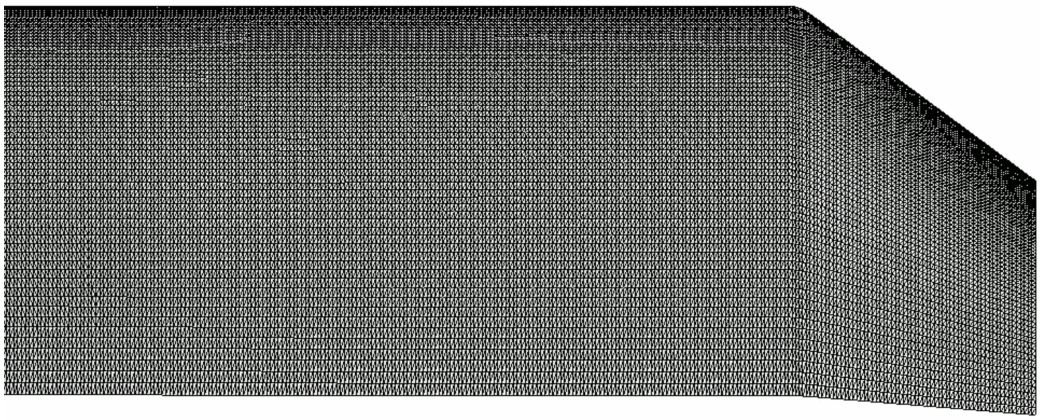

Figure 4.2: Generated grid of the blade surface.

to be set to a relatively low value equal to 0.001% of the chord length (1.5 e-06 m) with a growth rate equal to 1.2. The number of inflation layers is increased to properly capture the boundary layer. Inflation mesh refers to the prism layers growing from the blade surface mesh in order to generate elements that properly resolve the boundary layer over the airfoil.

Simulations were conducted using different number of inflation layers (10, 30, 45, 50, 70) for one representative case with a 10° blade pitch setting. The performance predictions related to these inflation specifications are collected and organized in Table 4.1 and plotted in Figure 4.3. It can be seen that the rotor performance indicators (thrust coefficient, power coefficient, and figure of merit), start to slightly stabilize after increasing the inflation layers to 50 layers. This value is kept for the other simulations set at different pitch angles as it achieves the best FM and properly resolves the boundary layer, without raising the number of mesh cells beyond the capabilities of the available computational power for this research.

Table 4.1: HVAB rotor performance predictions relative to the boundary layer grid.

Collective	Inflation Layers	Torque	Thrust	CP=CQ	CT	FM	Y+
10°	10	181,234	1092,852	0,000799	0,00814	0,65	0,545
10°	30	184,124	1108,64	0,000812	0,00826	0,653	0,519
10°	45	173,351	1111,833	0,000764	0,00828	0,697	0,514
10°	50	171,36	1117,224	0,000756	0,00832	0,71	0,745
10°	70	169,945	1109,863	0,000749	0,00827	0,709	0,519

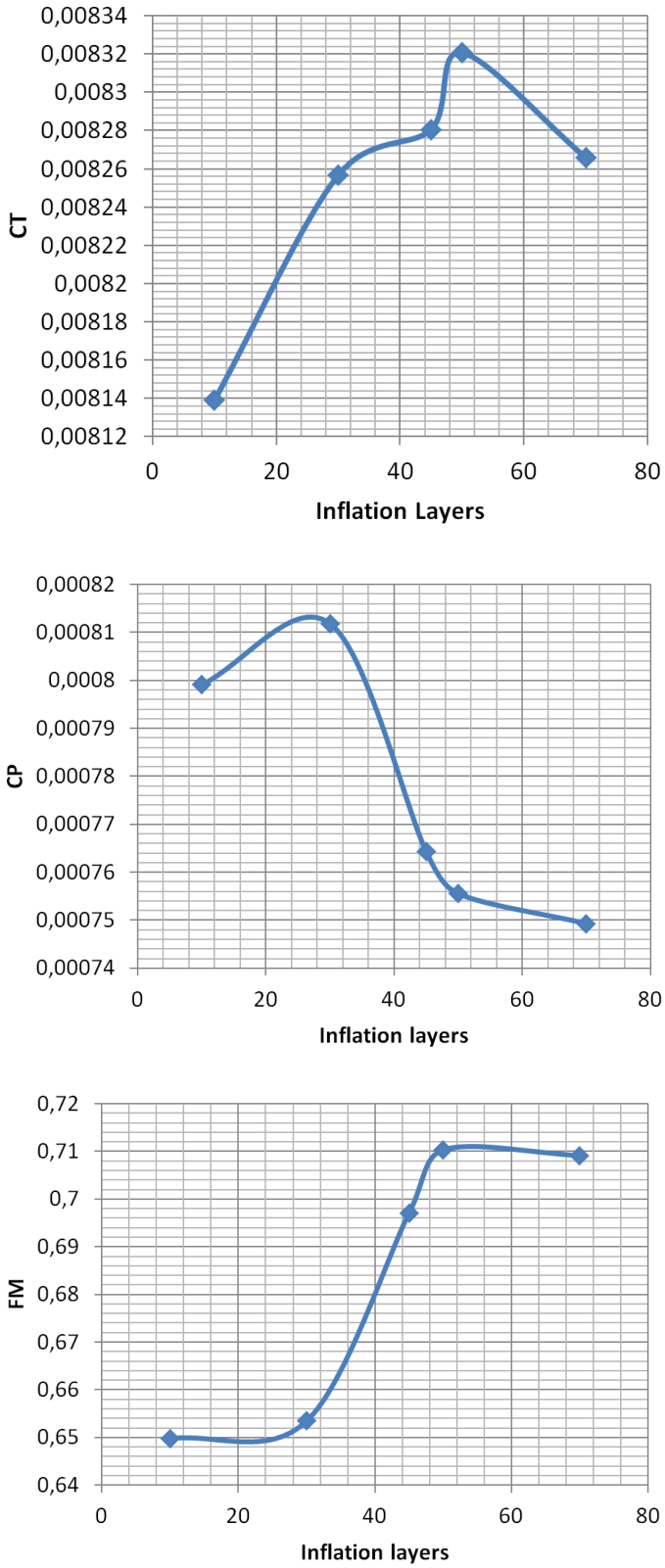

Figure 4.3: HVAB rotor numerical performance variation with the number of inflation layers.

The mesh of the boundary layer around the airfoil is shown in Figure 4.4. As mentioned above, prism layers cover the boundary layer region to ensure a proper resolution and mesh quality to accurately predict the flow behavior within the thin boundary layer. As discussed above, this can be achieved by properly adjusting the first layer thickness, the number of inflation layers and their growth rate.

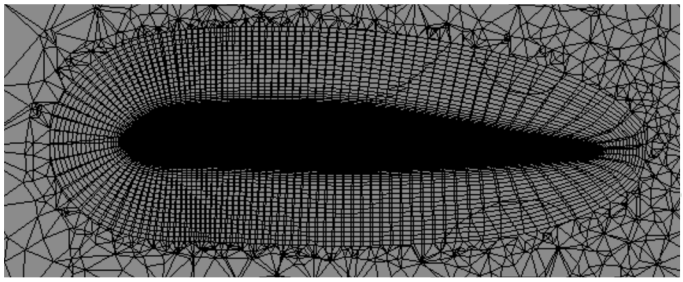

Figure 4.4: Inflation mesh of the boundary layer.

CHAPTER 5
RESULTS AND DISCUSSION

5.1 Performance Predictions

5.1.1 Convergence History

The numerical simulations of the HVAB rotor in hover are conducted for three different pitch settings: 6°, 8°, and 10°. The steady simulations are ran for a total number of iterations around 2500 iteration to ensure the proper convergence and the accuracy and relevance of the results used for the post-processing. Figure 5.1 shows two plots of the force and moment convergence tracking. One can notice that the thrust and torque are both starting to stabilize after 1200 iterations. The simulations are still ran for extra iterations to account for any further changes. The pressure-based solver type is used with a Coupled scheme and a Least Square Cell Based gradient. The second order upwind scheme is implemented for the spatial discretization of the momentum and energy equations along with a slight reduction of under-relaxation factors.

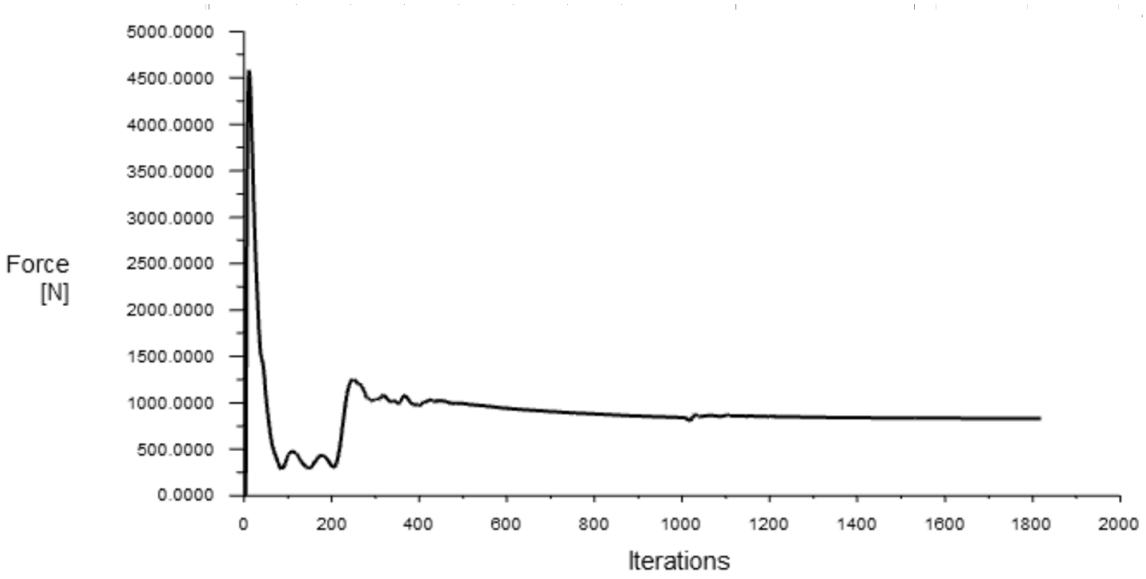

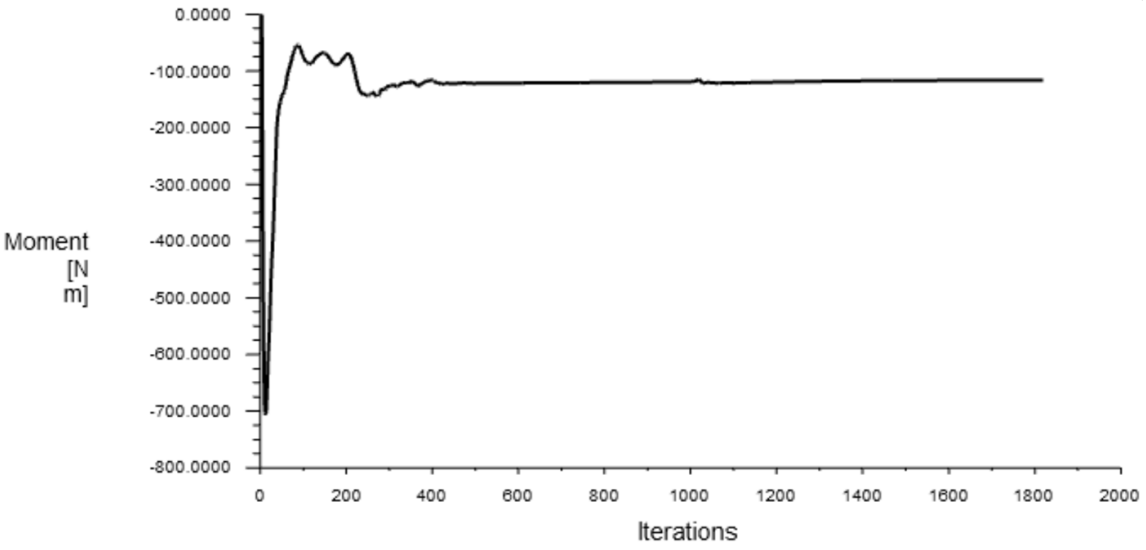

Figure 5.1: Force and Moment convergence for a representative case of Collective 8°.

5.1.2 Results and Validation

Table 5.1 compares the performance predictions of the previous work [1] to the improved data with a finer grid in terms of figure of merit, thrust, torque and their coefficients. As discussed previously, the Y+ is maintained below 1 at a value around 0.7 for all three pitch settings. Figure 5.2 translates this improvement into plots for better data visualization. The grid refinement and the proper resolution of the boundary layer lead to higher thrust and figure of merit predictions and lower power requirement.

Table 5.1: HVAB rotor coarse grid data (upper table) versus fine grid data (lower table).

Collective	Inflation Layers	Number of Cells	Torque	Thrust	CP=CQ	CT	FM	Y+
6°	10	~2,4M	76,809	562,14	0,000339	0,00419	0,566	~0,7
8°	10	~2,4M	120,072	820,549	0,000529	0,00611	0,638	~0,7
10°	10	~2,4M	178,79	1088,6	0,000788	0,00811	0,655	~0,7

Collective	Inflation Layers	Number of Cells	Torque	Thrust	CP=CQ	CT	FM	Y+
6°	50	~15M	77,341	575,506	0,000341	0,00429	0,582	0,718
8°	50	~15M	116,606	832,313	0,000514	0,0062	0,671	0,731
10°	50	~15M	171,36	1117,224	0,000756	0,00832	0,71	0,745

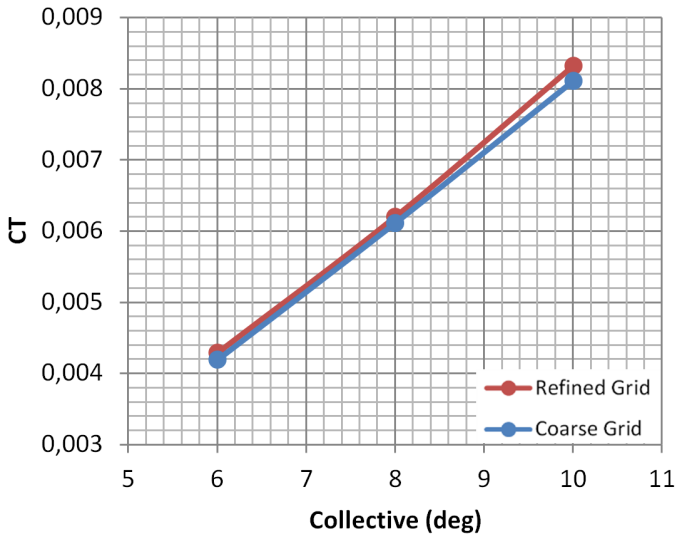

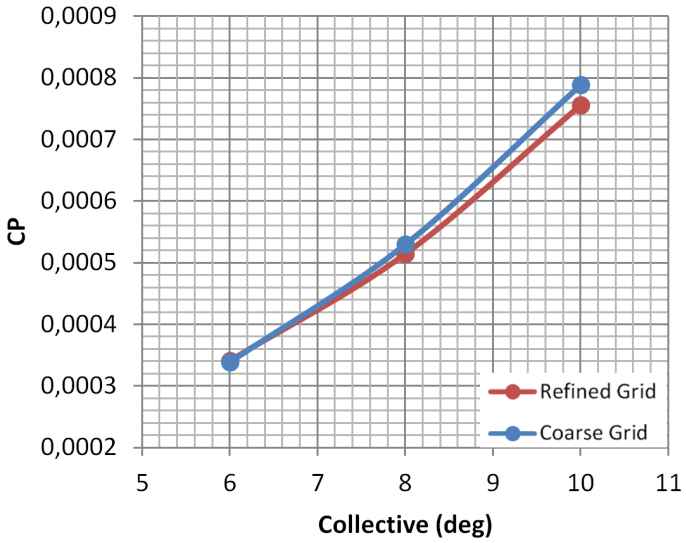

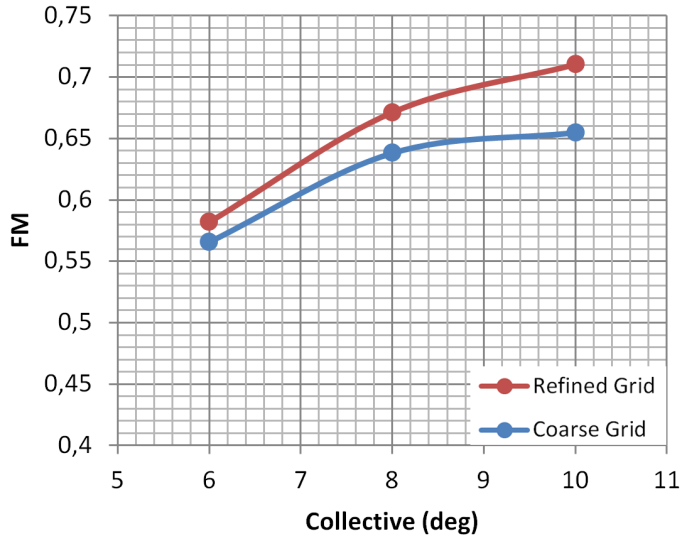

Figure 5.2: HVAB rotor fine grid versus coarse grid performance predictions.

The refined grid Fluent results are also plotted against the HVAB test data [4] and Jain's numerical findings [5]. Jain's work models the entire HVAB rotor using Helios and Overflow solvers with overset grids and a total cell count of 393 million cells. His numerical data are in good agreement with the disclosed HVAB test data for validation. Discrepancies with test data are more noticeable at higher blade pitch settings for both the Fluent Overflow/Helios solvers. The Fluent data depict a lower figure of merit and lower thrust and power coefficient compared to Jain's publication. Further refinement could potentially improve the Fluent data currently simulated using a total of 15 million grid cells. An estimated 10 to 20 fold increase in grid density is needed.

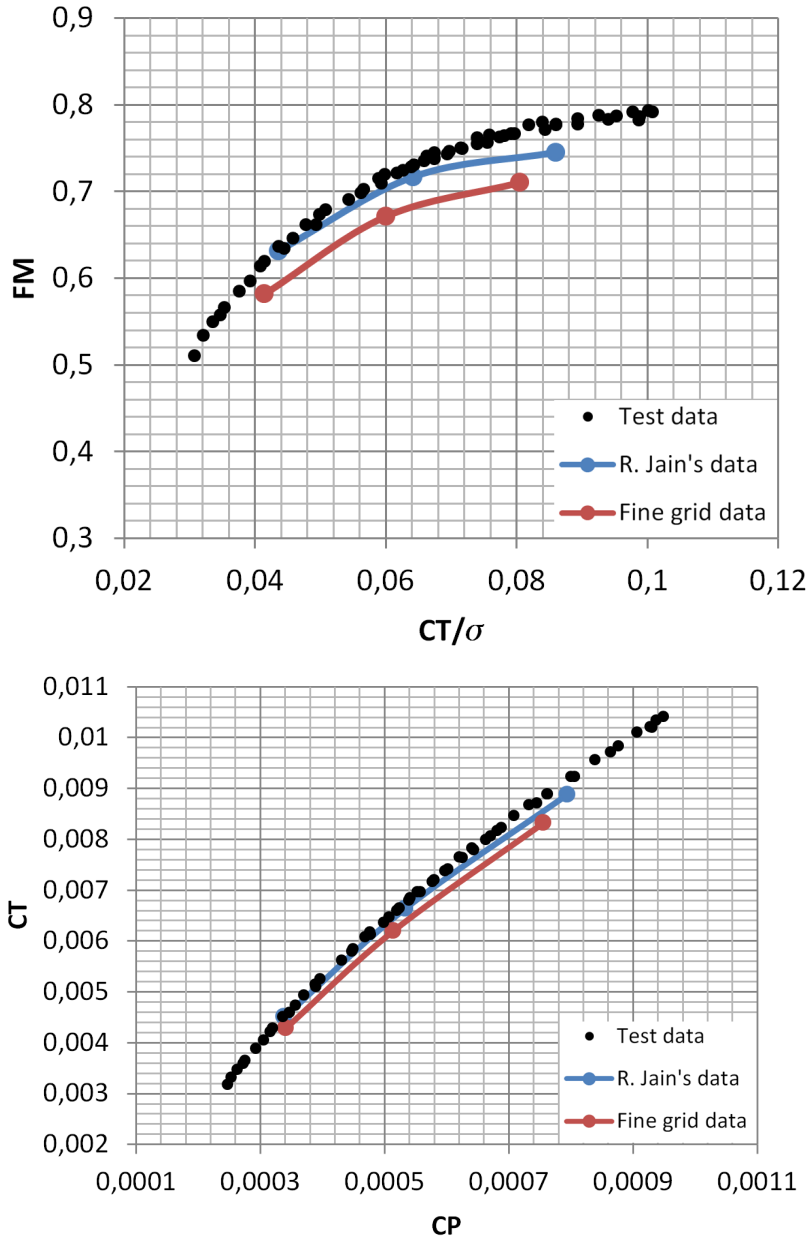

Figure 5.3: Comparison with HVAB test data and other numerical data.

The percentage error relative to the free transition HVAB test data is computed for a more accurate assessment of the performance predictions. The error is computed for both the fine grid and coarse grid predictions by curve fitting multiple test data points. As can be seen from Table 5.2, Table 5.3, and Table 5.4, refining the mesh from a total of 2.4 million cells to 15 million cells and properly resolving the grid of the boundary layer reduce the percentage error relative to the test data in terms of thrust generation, power requirement, and the rotor efficiency. All the percentage errors corresponding to the fine grid data are now one digit numbers.

Table 5.2: Thrust coefficient percentage error relative to HVAB test data.

	Coarse Grid		Fine Grid	
Collective	CT	% error relative to test data	CT	% error relative to test data
6	0,00419	7,03979	0,00429	4,830
8	0,00611	6,53136	0,00620	5,191
10	0,00811	7,13250	0,00832	4,691

Table 5.3: Power coefficient percentage error relative to HVAB test data.

	Coarse Grid		Fine Grid	
Collective	CP	% error relative to test data	CP	% error relative to test data
6	0,00034	7,99311	0,00034	5,803
8	0,00053	8,62542	0,00051	3,754
10	0,00079	16,33617	0,00076	8,178

Table 5.4: Figure of merit percentage error relative to HVAB test data.

	Coarse Grid		Fine Grid	
Collective	FM	% error relative to test data	FM	% error relative to test data
6	0,00419	7,41387	0,00429	5,497
8	0,00611	7,95282	0,00620	3,631
10	0,00811	14,05370	0,00832	7,573

5.2 Induced Power and Velocity Inflow

Power can be divided into three main parts: induced, profile, and parasite power with the first two accounting for the largest contributions.

$$C_P = C_{Pinduced} + C_{Pprofile} + C_{Pparasite} \tag{5.1}$$

$$C_{Pinduced} = \kappa \lambda_i C_T \tag{5.2}$$

κ is the non-uniform flow and tip loss factor and λ_i refers to the induced velocity coefficient. In hover condition:

$$\lambda_i = \sqrt{\frac{C_T}{2}} \tag{5.3}$$

Therefore,

$$C_{Pinduced} = \kappa \sqrt{\frac{C_T}{2}} C_T \tag{5.4}$$

The HVAB induced power coefficient is calculated for all three simulations. The induced power increases with the increase of thrust generation, and the resulting non-uniform and tip loss factor κ is found to be equal to 1.31. The typical value for κ is taken to be 1.15. Thus, the computed κ is higher than the ideal value. This difference is found to be mainly due to the radial and azimuthal variation as seen from the velocity inflow in Figure 5.5. The velocity component normal to the rotor disk is used as the variable for the velocity inflow contour at a distance of 1c above the rotor (with c being the chord length). The

non-linearity of the induced velocity and the upwash detected at the last 5% of the rotor radius lead to the overestimation of κ.

Table 5.5: Induced power and thrust coefficients.

Collective	CP induced	CT
6°	0,000270	0,00428
8°	0,000446	0,00620
10°	0,000683	0,00827

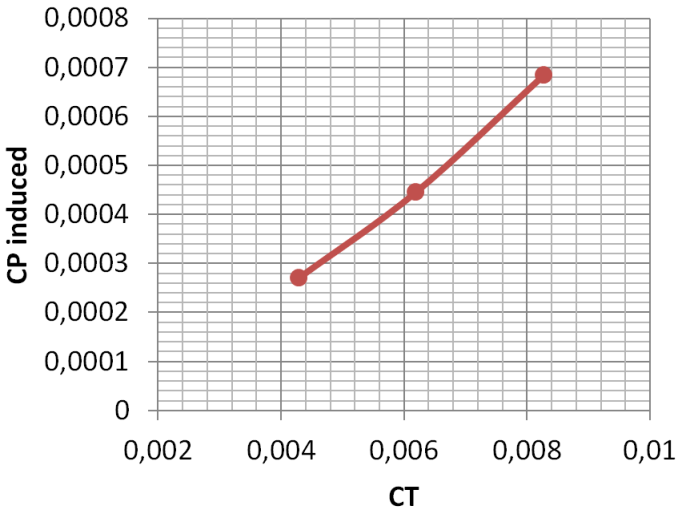

Figure 5.4: Induced power coefficient versus thrust coefficient.

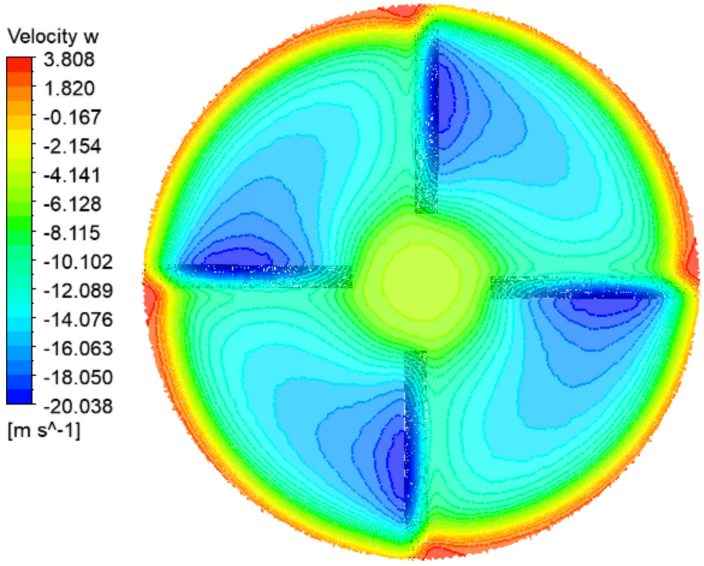

Figure 5.5: Velocity inflow one chord above the rotor disk (10° pitch reference case).

5.3 Spanwise Lift Distribution

The lift per unit span is plotted at 11 radial sections of the blade to visualize the lift generation variation from the root to the tip of the rotor blade for each of the three pitch settings. The increase of the pitch angle leads to an increase of the angle of attack which generates additional lift. It can be seen that the sectional lift value increases from root to tip with a peak around R/r = 0.95 followed by a drop towards the blade tip region due to the tip vortex formation. This drop is steeper at lower pitch settings. Rotors generate more lift at the fast-moving blade region compared to the slow-moving root region.

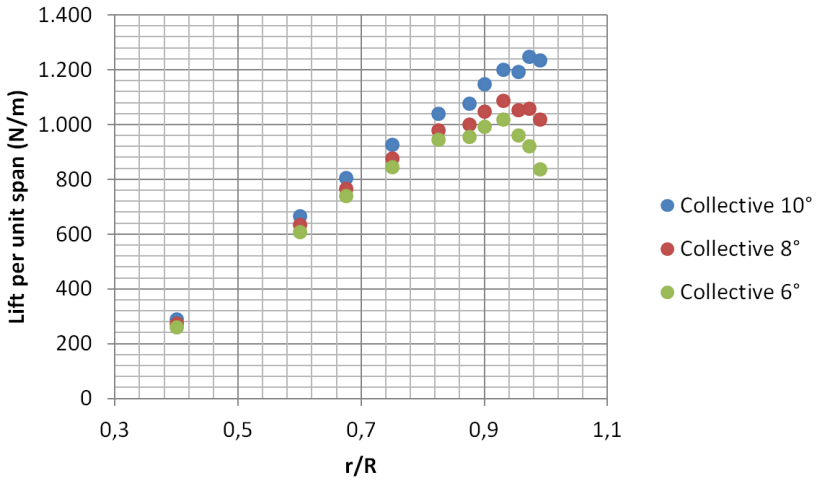

Figure 5.6: Spanwise lift distribution for three pitch settings.

5.4 Surface Pressure Distribution

Surface pressure distributions are plotted for the three collective pitch settings and at different radial sections of the blade: r/R= 0.4, 0.6, 0.675, 0.75, 0.825, 0.875R, 0.9, 0.93, 0.955, 0.973, 0.99, with R being the rotor radius and r the distance from the rotor center. The improved Fluent Cp results (in red) are plotted against the previous results (in blue) to highlight the improvement of the suction peak at the leading edge which was previously underestimated (see Figure A.2). The improved Cp distributions are also plotted against the numerical results of two different publications (in black) [2] [6]. The comparisons at the pitch setting 8° are presented in Figure A.2 and Figure A.4 as a representative case. The rest of the plots corresponding to the collective angles 6° and 10° are presented in Appendix A. From the first comparison, one can notice the improvement at the suction peak after the mesh adjustments. The new suction peaks (in red) are still slightly underestimated in some radial sections especially towards the tip (mainly the last four radial sections). The second comparison introduces the fine grid Fluent Cp data versus the findings of a second paper [6]. Good agreement can be concluded overall except at the last three radial sections where the entire Fluent upper Cp distribution curve is shifted downward. Both comparisons indicate that further improvement is to be sought at least for the last four radial locations.

In an attempt to overcome these discrepancies, the blade tip region has been further refined by using a sphere of influence around the tip region and refining the mesh of the tip region surface. Implementing these changes increased the cell count up to 22 million cells. Nonetheless, the performance predictions and surface pressure distributions were not subjected to any significant change. A more significant refinement is required to improve the predictions with a 10 to 20 fold increase in grid density estimated based on the grid cell count of other similar publications.

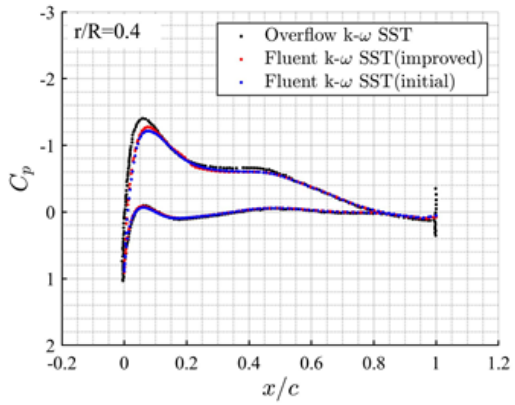
r/R=0.4
Overflow k-ω SST
Fluent k-ω SST(improved)
Fluent k-ω SST(initial)
C_p
x/c

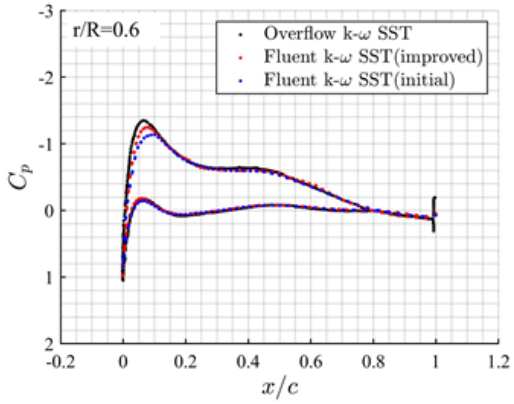
r/R=0.6
Overflow k-ω SST
Fluent k-ω SST(improved)
Fluent k-ω SST(initial)
C_p
x/c

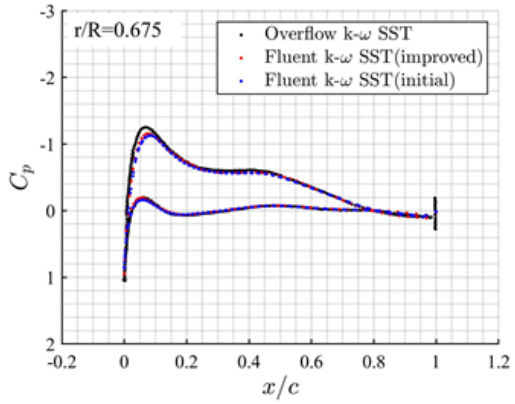
r/R=0.675
Overflow k-ω SST
Fluent k-ω SST(improved)
Fluent k-ω SST(initial)
C_p
x/c

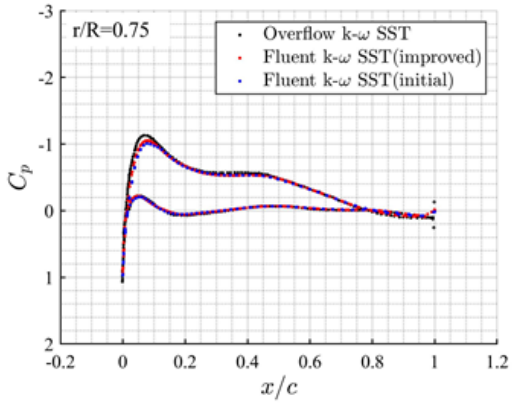
r/R=0.75
Overflow k-ω SST
Fluent k-ω SST(improved)
Fluent k-ω SST(initial)
C_p
x/c

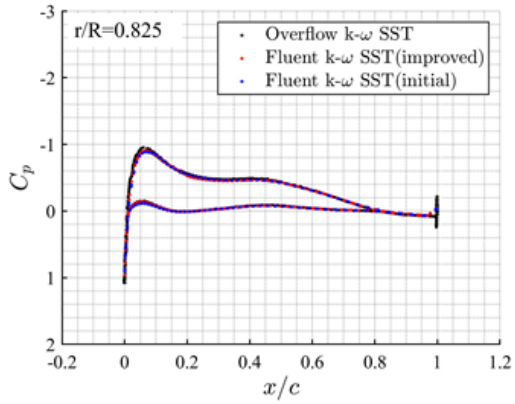
r/R=0.825
Overflow k-ω SST
Fluent k-ω SST(improved)
Fluent k-ω SST(initial)
C_p
x/c

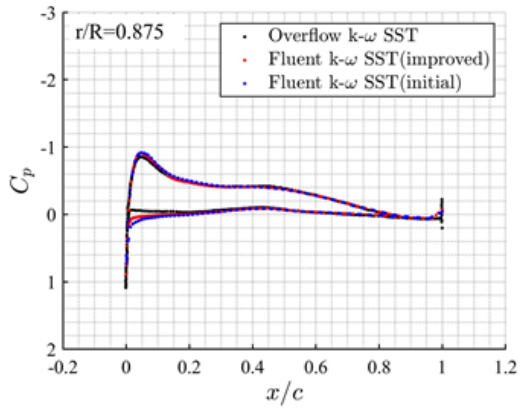
r/R=0.875
Overflow k-ω SST
Fluent k-ω SST(improved)
Fluent k-ω SST(initial)
C_p
x/c

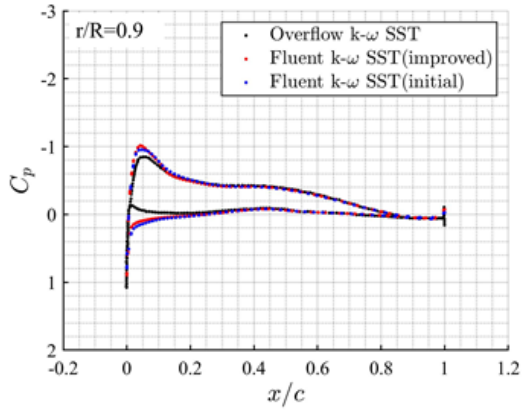
r/R=0.9
Overflow k-ω SST
Fluent k-ω SST(improved)
Fluent k-ω SST(initial)
C_p
x/c

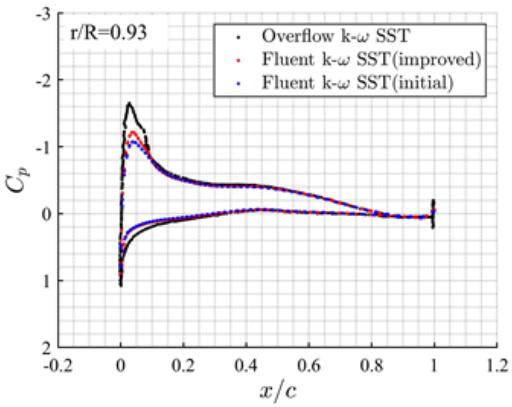
r/R=0.93
Overflow k-ω SST
Fluent k-ω SST(improved)
Fluent k-ω SST(initial)
C_p
x/c

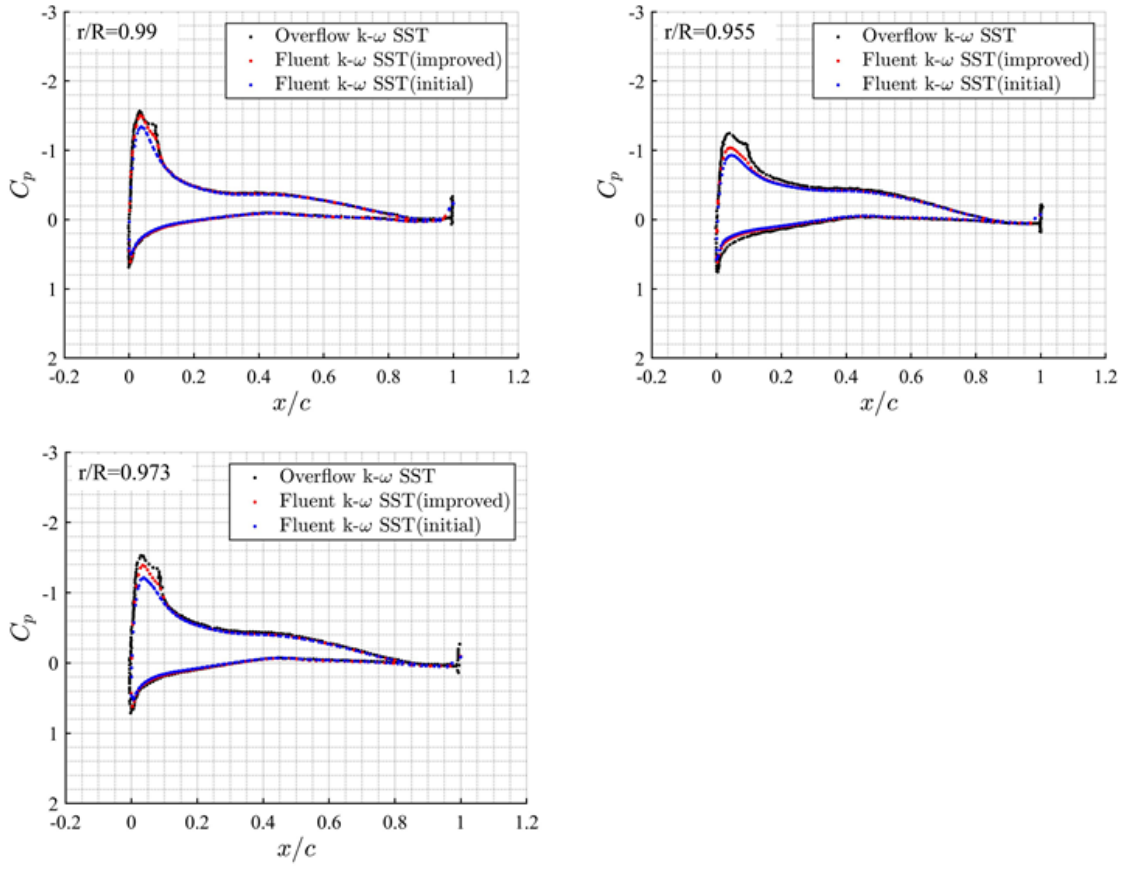

Figure 5.7: Surface pressure distribution plots at 8° pitch setting (first comparison).

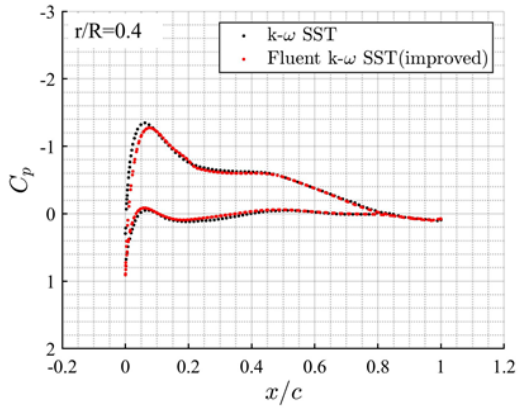
r/R=0.4
k-ω SST
Fluent k-ω SST(improved)
C_p
x/c

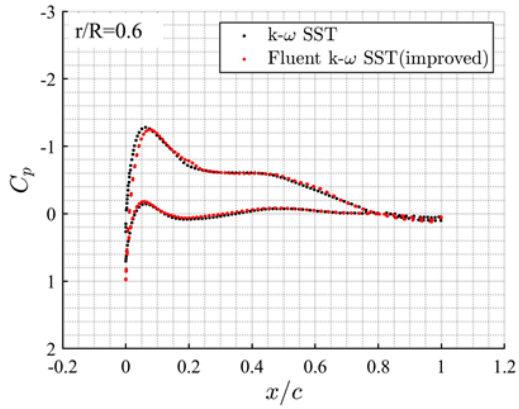
r/R=0.6
k-ω SST
Fluent k-ω SST(improved)
C_p
x/c

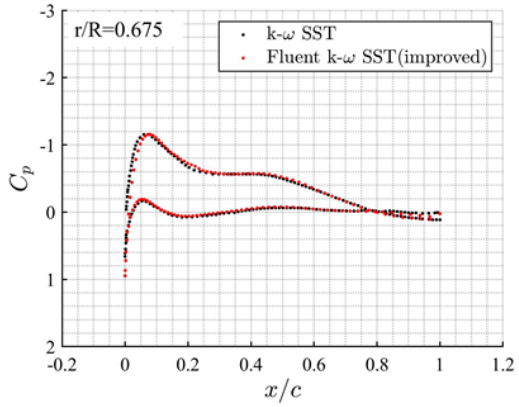
r/R=0.675
k-ω SST
Fluent k-ω SST(improved)
C_p
x/c

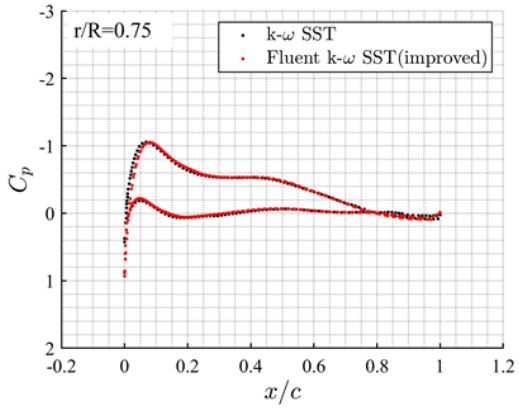
r/R=0.75
k-ω SST
Fluent k-ω SST(improved)
C_p
x/c

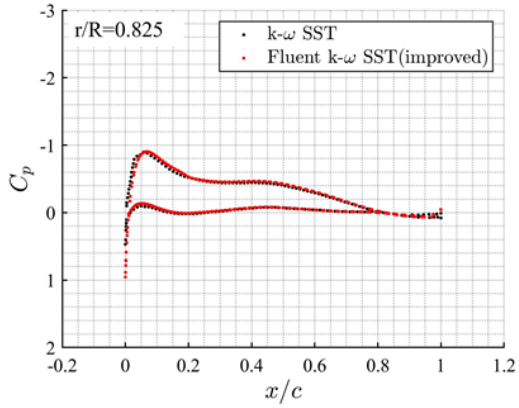
r/R=0.825
k-ω SST
Fluent k-ω SST(improved)
C_p
x/c

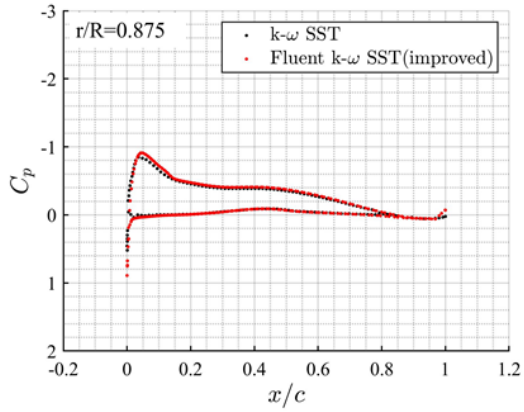
r/R=0.875
k-ω SST
Fluent k-ω SST(improved)
C_p
x/c

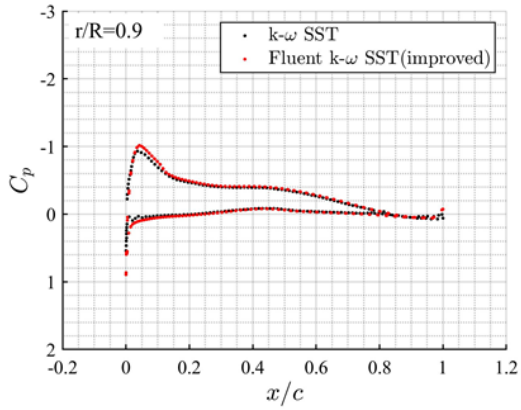
r/R=0.9
k-ω SST
Fluent k-ω SST(improved)
C_p
x/c

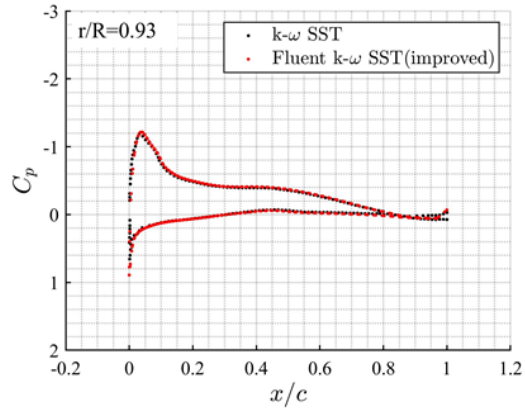
r/R=0.93
k-ω SST
Fluent k-ω SST(improved)
C_p
x/c

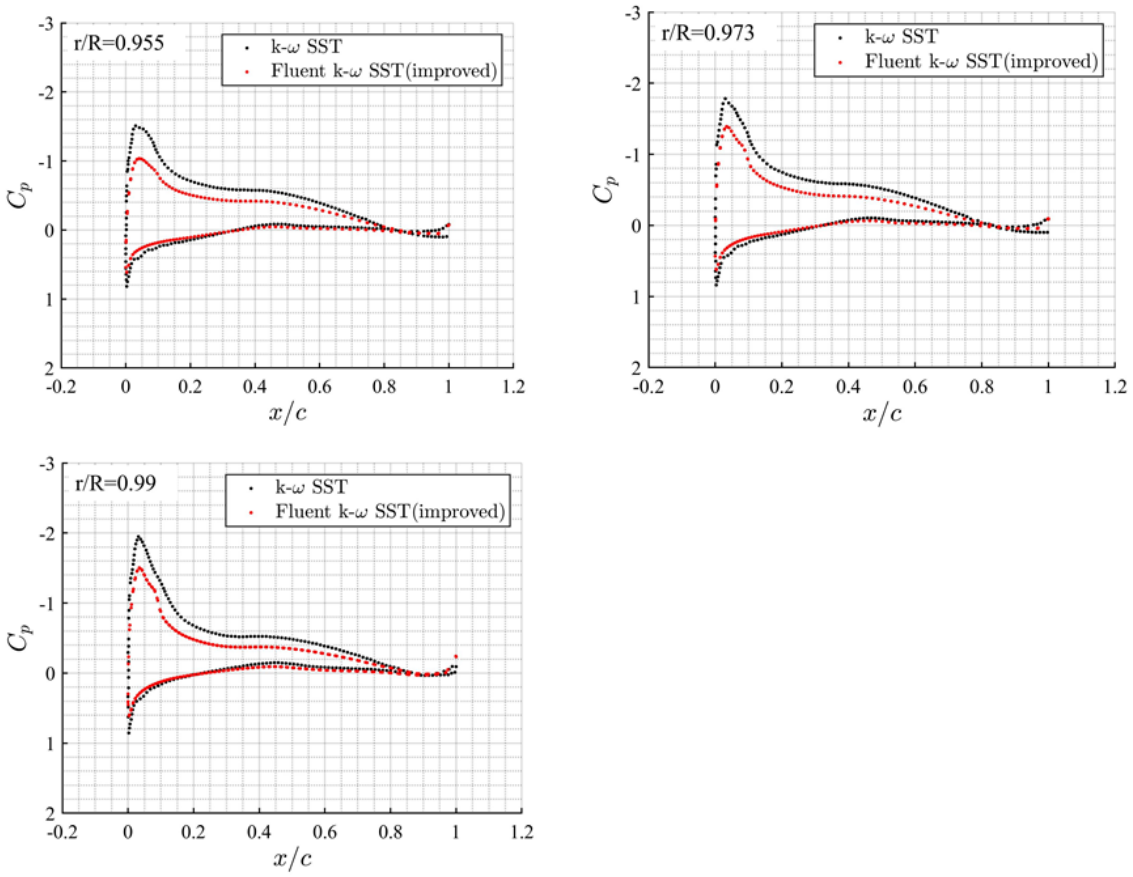

Figure 5.8: Surface pressure distribution plots at 8° pitch setting (second comparison).

5.5 Pressure and Velocity Contours

Pressure and velocity contours are discussed within this chapter to visualize their behavior at different radial blade sections. The pressure levels across these sections (r/R= 0.4, 0.675, 0.825, 0.973) are depicted in Figure 5.9. The lower surface experiences higher pressure compared to the upper surface which creates the pressure differential needed to generate lift. From root to tip, the pressure decreases on the upper surface and increases on the lower surface as shown by the pressure increase at the stagnation point where the pressure is at its highest and velocity is zero. One can also detect how the pressure grows on the lower surface and drops on the upper surface with the increase of the pitch setting. This behavior leads to a larger pressure differential and thus higher generated lift.

When a particle is moving with a certain velocity while being surrounded by a decreasing pressure field, it will accelerate since there will be a net force in the same direction as the velocity. In contrast, when it is surrounded by an increasing pressure field then it is bound to decelerate. Hence, the pressure distribution in Figure 5.9 can be easily translated in terms of velocity (see Figure 5.10). The increase in pitch leads to an increase of velocity, and the tip region of the blade experiences the highest velocities while the lowest velocities are towards the blade root.

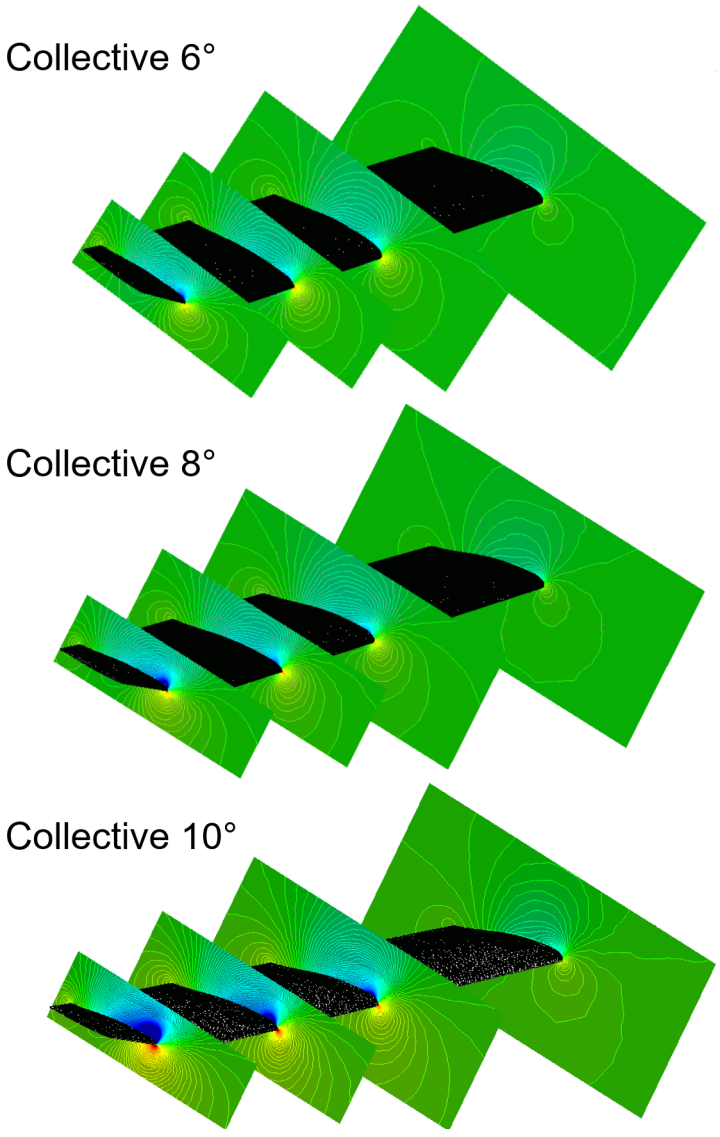

Figure 5.9: Pressure distribution contours for three pitch settings.

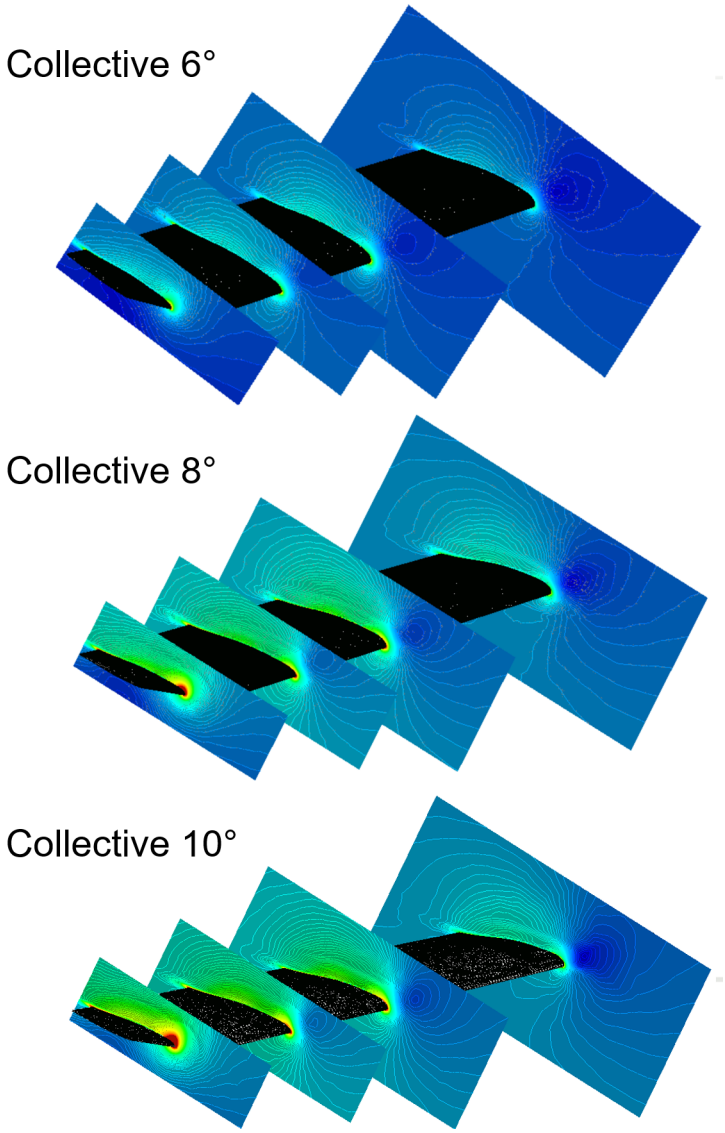

Figure 5.10: Velocity distribution contours for three pitch settings.

CHAPTER 6
FLOW TRANSITION

Boundary layer is a thin viscous fluid layer near a body surface such that the velocity is equal to zero at the surface (no slip condition), and is equal to the freestream velocity far enough from the surface. The proper modelling of boundary layers allows a better understanding of stalling behavior, skin friction drag, and so on. The flow, at first laminar in nature, can be subjected to separation which makes it briefly transitional (laminar and turbulent) before the flow eventually becomes turbulent. One of the features of turbulent boundary layers is the steeper velocity gradient at the wall accompanied by higher shear stress in contrast to laminar boundary layers.

In this work, the transition locations are identified by detecting the sudden jump in the skin friction coefficient and the intermittency values along the upper and lower surfaces of the HVAB blade. This can be achieved by generating the contours of those quantities and visualizing their sudden rise locations indicating the start of flow transition.

6.1 Intermittency

Intermittency is defined as the time percentage during which the flow is turbulent. An intermittency value of 0 indicates laminar flow while a value of 1 designates turbulent flow. Figure 6.1 and Figure 6.2 allow the identification of the sudden value jump in intermittency which serves as an indicator of transition occurrence within the flow. The red region refers to the turbulent region while the blue one represents the laminar region. Here, the intermittency contours are focused on the region between the middle of the blade and its tip. Looking at the upper surface contours on the left side of Figure 6.1, one can visualize how

the transition locations move closer to the leading edge with the increase of the pitch setting. The Fluent data are once again compared to Jain's findings presented on the right side of Figure 6.1 and Figure 6.2 [5]. The transition predictions on the upper surface are very similar to the comparative contours at the tip region of the blade. The Fluent predictions away from the tip show some discrepancies especially at lower pitch settings along with the presence of some abnormal streaks towards the middle of the blade. These sudden jumps in values are not physically possible since the transition points would realistically vary in a smoother manner in the radial direction instead of these sudden variations.

Conversely, on the lower surface (see the left contours of Figure 6.2), the transition locations across the blade move closer to the trailing edge instead with the increase of the collective pitch. In other words, due to the increase of the collective, the laminar region decreases on the upper surface while the turbulent region decreased on the lower surface. A correlation between the Mach number and transition onset locations can be established. In their analysis of the HVAB rotor, Kwon and Park concluded that the increased local Mach number on the upper blade surface is responsible of the transition locations moving closer to the leading edge. In contrast, the reduced Mach number on the lower surface causes the transition locations to move away from it [7]. The streaks mentioned above appear on the lower surface as well. The reason behind the presence of such significant fluctuations is yet to be determined.

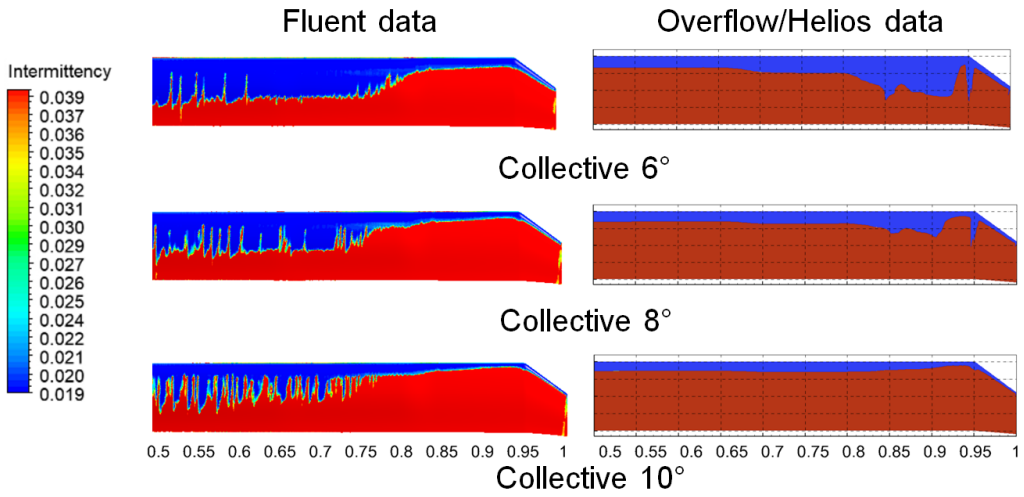

Figure 6.1: Comparison of HVAB transition predictions using skin friction coefficient between Fluent and Overflow/Helios solvers (upper surface).

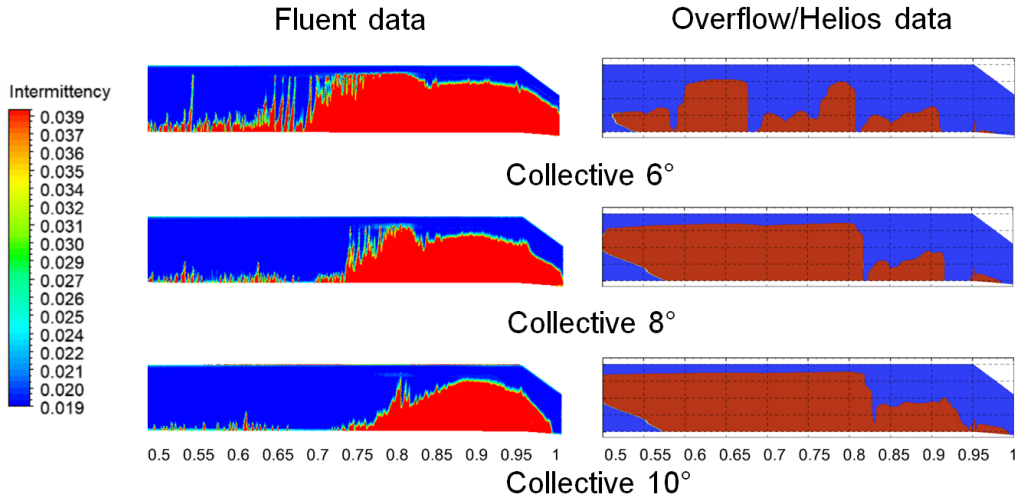

Figure 6.2: Comparison of HVAB transition predictions using skin friction coefficient between Fluent and Overflow/Helios solvers (lower surface).

6.2 Skin Friction Coefficient

Skin friction coefficient is a non-dimensional parameter characterizing boundary layer flows relying on wall shear stress. The contours in Figure 6.3 are generated for the entire blade length. The transition locations identified using the skin friction coefficient are identical to the ones acquired using intermittency. In other words, the skin friction coefficient value jumps (see Figure 6.3) occur at the same locations as the intermittency value jumps (see Figure 6.1 and Figure 6.2), as expected, indicating flow transition. As a consequence of the increase of the pitch setting, these locations are getting closer to the leading edge on the upper surface, and away from it on the lower blade surface. Similarly to the intermittency contours, the Fluent skin friction contours also show some streaks in the middle portion of the blade indicating high fluctuations of skin friction coefficients which is not a realistic flow behavior. Further investigation is required to identify the cause of these sudden value jumps in order to accurately predict the transition locations.

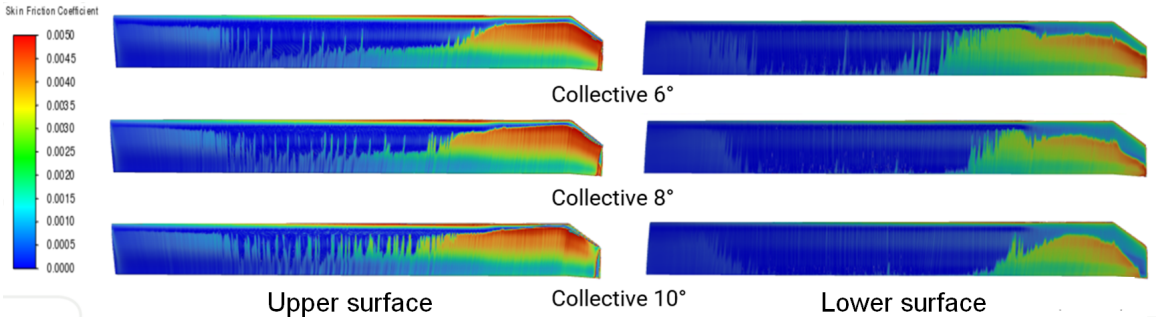

Figure 6.3: HVAB transition predictions using skin friction coefficient.

CHAPTER 7
VORTICITY

Vortices are combinations of spinning elements in a fluid while vorticity is a measure of the local rotational motion of these fluid particles. Its mathematical representation can be formulated as the curl of the velocity vector:

$$\Omega = \Delta \times U \tag{7.1}$$

It can also be represented as twice the angular velocity of a fluid particle:

$$\Omega = 2\omega \tag{7.2}$$

7.1 Rotor Inner Wake

The blade tip vortex system is one of the most important attributes related to the wake of helicopter rotors. Properly predicting the wake is yet considered challenging to achieve. Generating vorticity contours allows to visualize the structure of the HVAB rotor wake in hover condition. From Figure 7.1 one can notice the improved quality of the vorticity contour compared to the findings of the previous work for the representative case of collective pitch 10°. The contours are applied to the vertical plane located right behind the trailing edge of the HVAB blade at a distance of 2c away from the quarter chord point (with c being the chord length). The colors are more vibrant and the structure is better predicted now that the mesh has been refined which improves the accuracy of the current findings. The contour is generated using a Q-criterion level equal to 1.5^{-5} and a velocity curl range between 0 and 500 (1/sec). Vortex sheets can be defined as a surface across which there is a velocity discontinuity. In all the following vorticity contours, the left end of the blade is

the tip and the right one is the root. One can visualize how the outer edge of these vortex sheets in Figure 7.1 is descending faster compared to the leading edge as expected from the theory (see Figure 7.2). The individual tip vortices are more visible and intense with the collective increase.

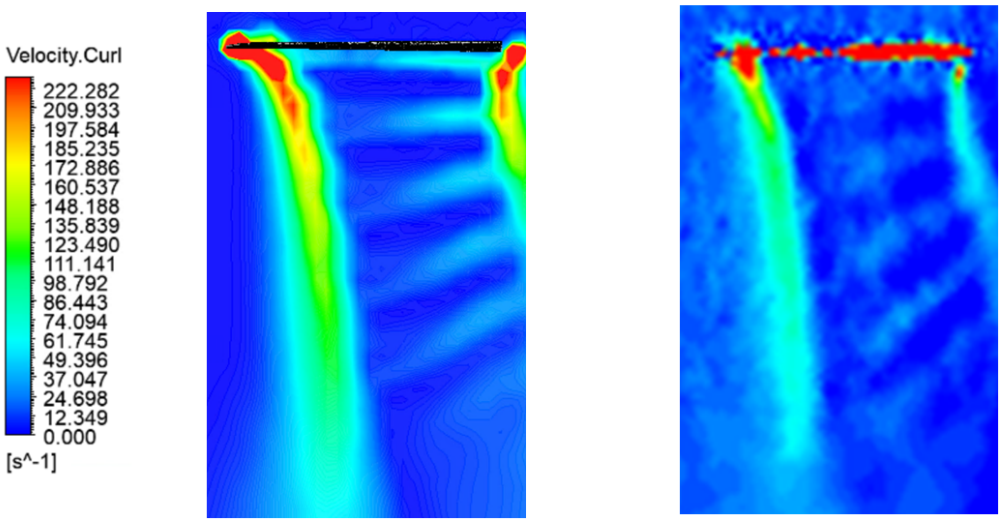

Figure 7.1: Fine grid rotor wake (left image) versus coarse grid rotor wake [1] (right image).

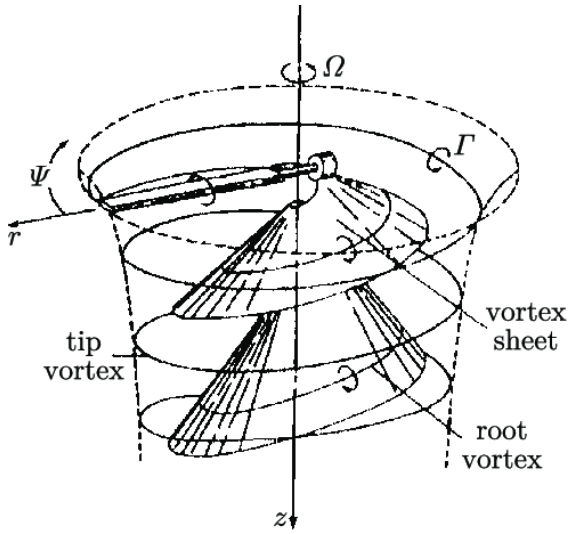

Figure 7.2: Rotor wake structure for one rotor blade. [8]

Figure 7.3 exhibits an increase in vortical strength with the increase of the blade pitch setting. The vortex sheets can be visualized as well, and are more the visible and pronounced with the increase of the pitch setting.

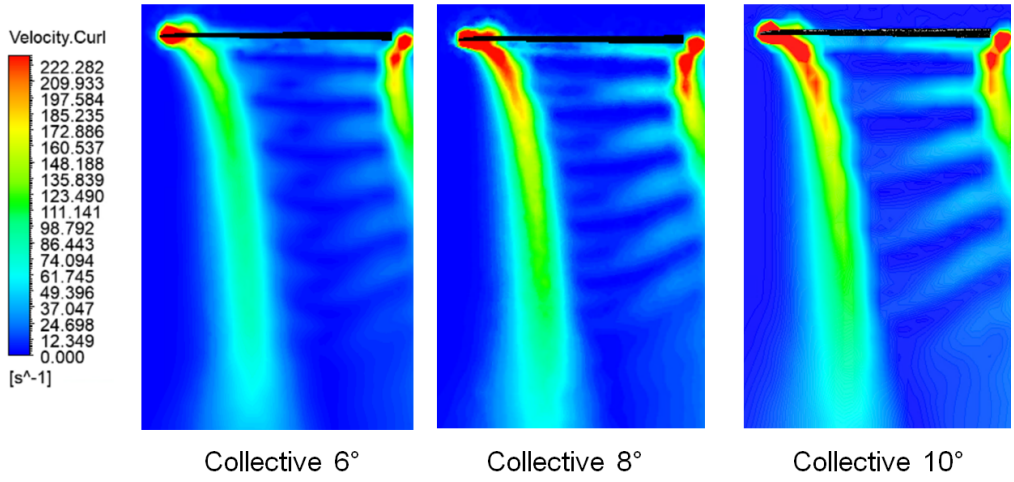

Figure 7.3: Rotor inner wake corresponding to different pitch settings.

The rotor wake corresponding to the reference case of 10° pitch setting is compared to Jain's data [5] (see the right image of Figure 7.4) which models the entire HVAB rotor using Helios and Overflow solvers with overset grids and a total cell count of 393 million cells as mentioned previously. The vortex sheets are visible both on the Fluent contour (left image) and on the comparative vorticity contour (right image). According to Jain, the generated tip vortices are clean and stable for the first three blade passages, and tend to break down beyond that [5]. Nonetheless, the Fluent vortex structures are not as defined or precise as the right image. Further refinement could be implemented in the rotor wake region and around the blade tip to possibly achieve cleaner and more defined individual tip vortices and allow more relevant conclusions to be drawn concerning the rotor wake and tip vortex structure.

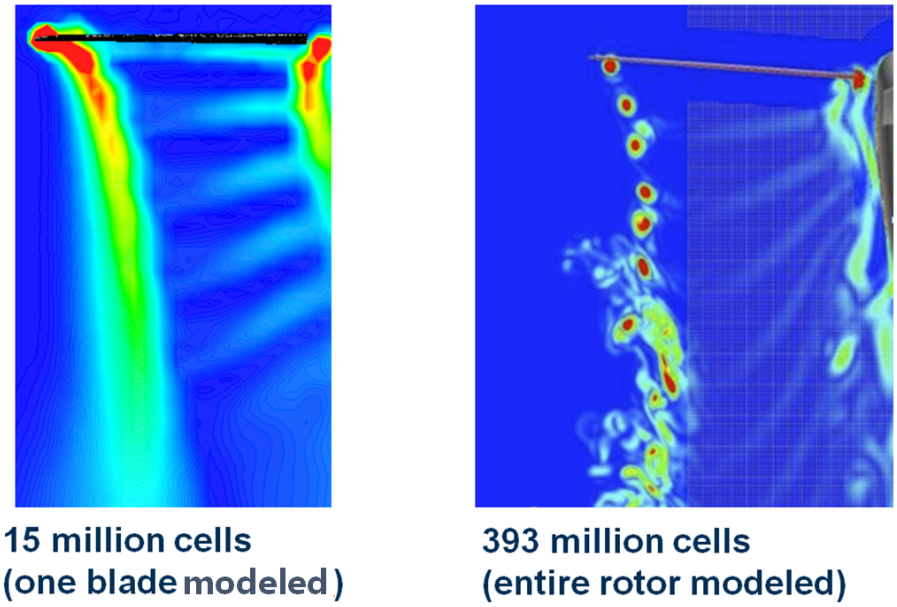

Figure 7.4: Fluent rotor wake (left image) versus other publication [5] (right image)

7.2 Near Wake Tip Vortex

For the three pitch settings simulated, our near wake tip vortex (see the images above of Figure 7.5) is compared to the vortex displayed within the images below [6] of the same figure. Increasing the blade pitch angle leads to an increase of vorticity at the blade tip. The difference in magnitudes in the legends of the two sets of images is solely due to the images above using the velocity curl to define vorticity with the unit 1/sec while the images below are expressed in terms of normalized vorticity.

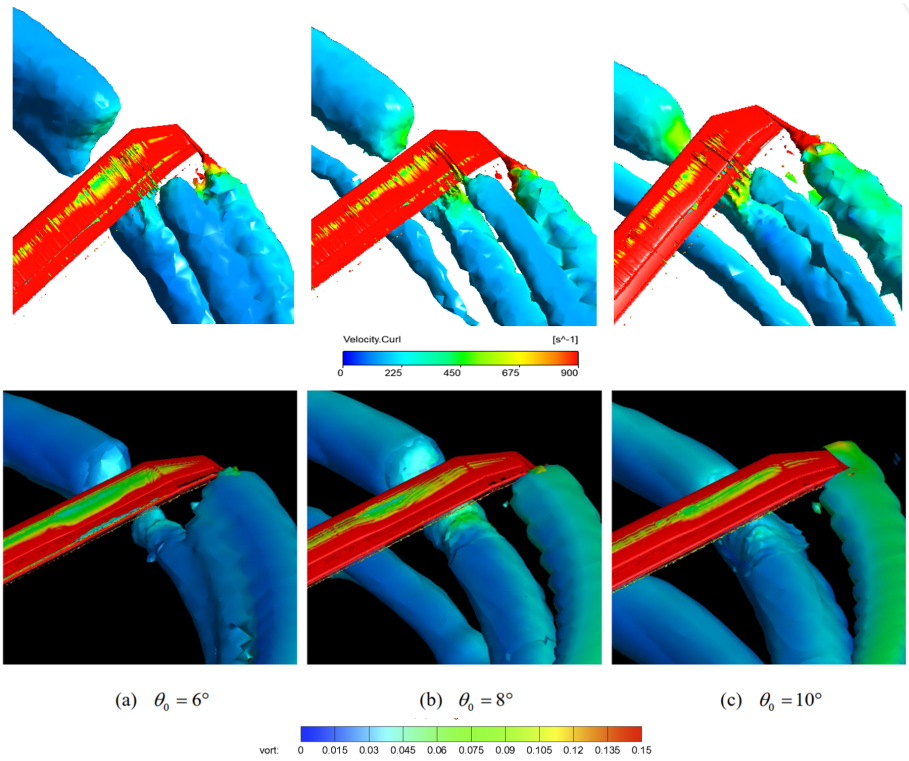

Figure 7.5: Fluent near wake tip vortex versus other publication [6].

CHAPTER 8
CONCLUSION AND RECOMMENDATIONS

The current work discusses the improved CFD analysis of the HVAB rotor in hover condition. The accuracy of the performance predictions has improved, and the vortex structures are visualized with higher quality and more defined individual tip vortices which were not visible in the previous work. Further improvement could still be sought in the future by refining the grid even further with a focus on the blade tip region in order to achieve better surface pressure distributions at the suction peaks of the tip sections, cleaner and more defined individual tip vortices and overall improved performance predictions. The estimated running time of one simulation would then be about 720 to 1440 hours (150 to 300 million grid cells) using the same computational power available (6 solver processes) on a desktop with 6 cores and 12 logical processors. Adaptive meshing could also be an advantageous method to implement in order to achieve local refinement depending on the solution of the simulation. Aside from the grid refinement, further investigation remains necessary to identify the source of the abnormal streaks detected on the intermittency and skin friction coefficient contours and to eliminate them for more accurate transition location predictions. The level of accuracy of this work remains limited by the computational power available and the running time of simulations.

A potential continuation or improvement of this project could include further refinement of the grid as discussed above and possibly the use of a different CFD solver for comparative purposes. The performance predictions would then be improved, and the close interaction between passing blades and tip vortices would be analyzed in a more advanced manner. Transient time simulations could be conducted as well to study the temporal development of rotor wake structures at successive wake ages.

Appendices

APPENDIX A

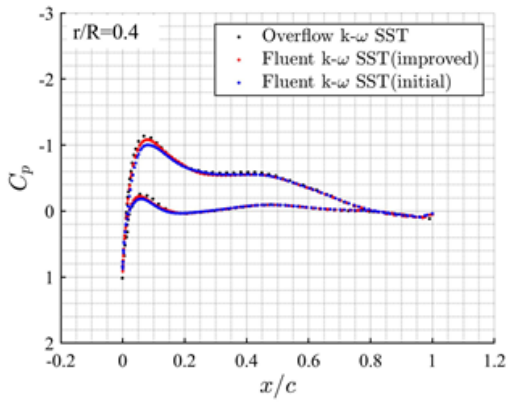
r/R=0.4
Overflow k-ω SST
Fluent k-ω SST(improved)
Fluent k-ω SST(initial)
C_p
x/c

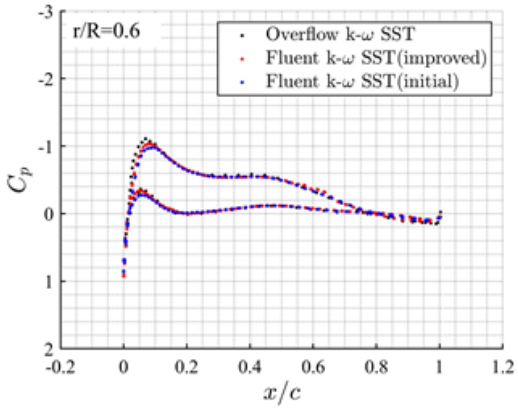
r/R=0.6
Overflow k-ω SST
Fluent k-ω SST(improved)
Fluent k-ω SST(initial)
C_p
x/c

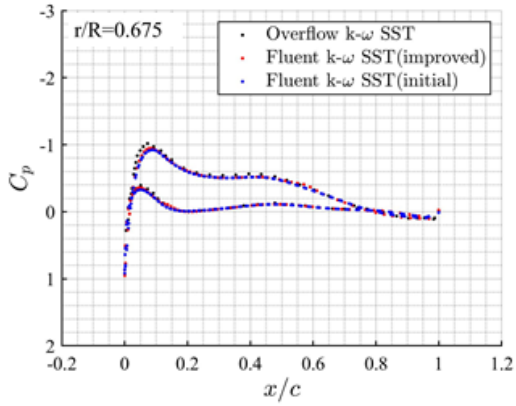
r/R=0.675
Overflow k-ω SST
Fluent k-ω SST(improved)
Fluent k-ω SST(initial)
C_p
x/c

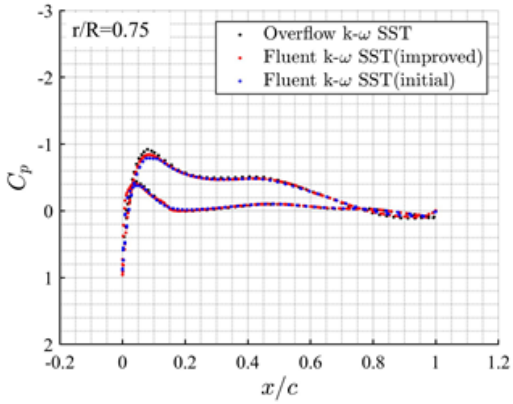
r/R=0.75
Overflow k-ω SST
Fluent k-ω SST(improved)
Fluent k-ω SST(initial)
C_p
x/c

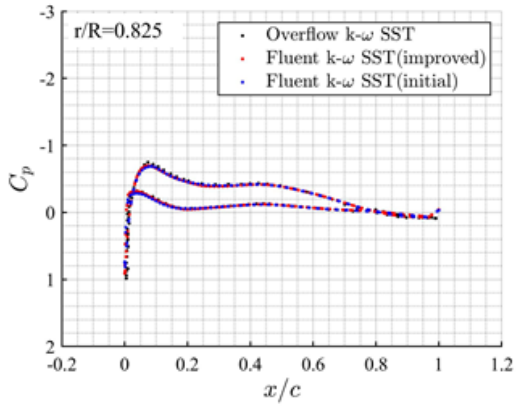
r/R=0.825
Overflow k-ω SST
Fluent k-ω SST(improved)
Fluent k-ω SST(initial)
C_p
x/c

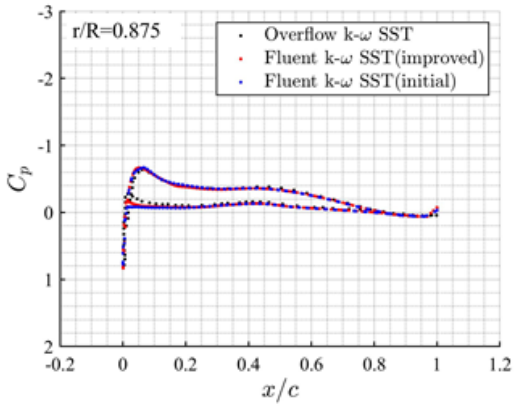
r/R=0.875
Overflow k-ω SST
Fluent k-ω SST(improved)
Fluent k-ω SST(initial)
C_p
x/c

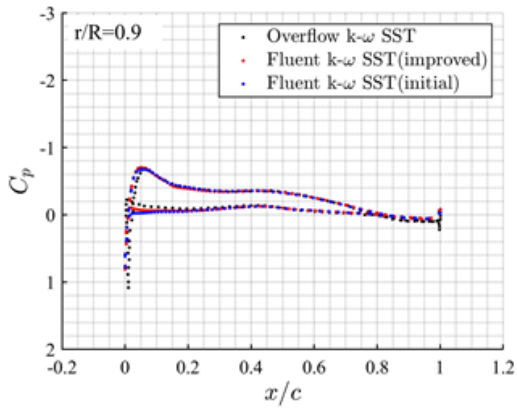
r/R=0.9
Overflow k-ω SST
Fluent k-ω SST(improved)
Fluent k-ω SST(initial)
C_p
x/c

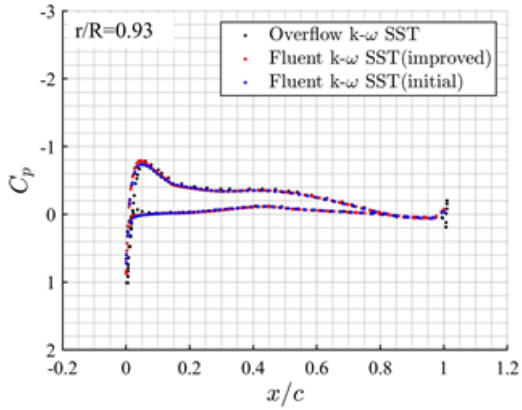
r/R=0.93
Overflow k-ω SST
Fluent k-ω SST(improved)
Fluent k-ω SST(initial)
C_p
x/c

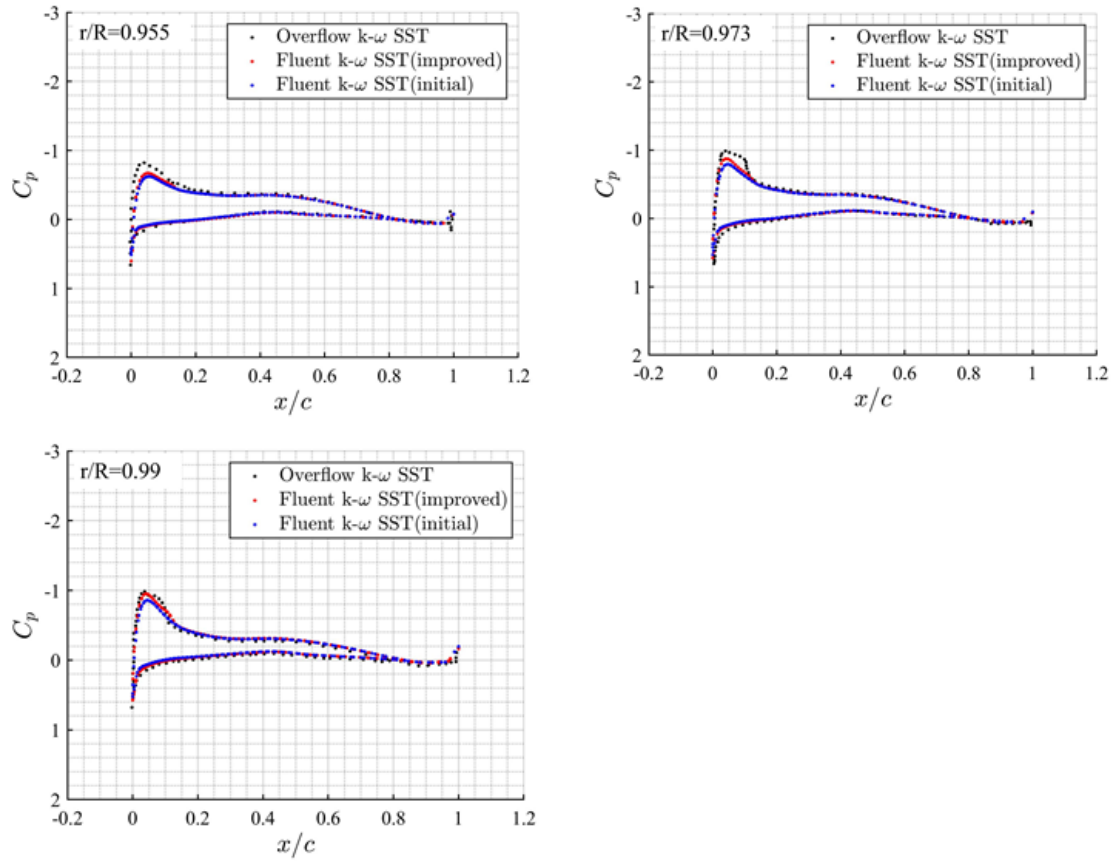

Figure A.1: Surface pressure distribution plots at 6° pitch setting (first comparison).

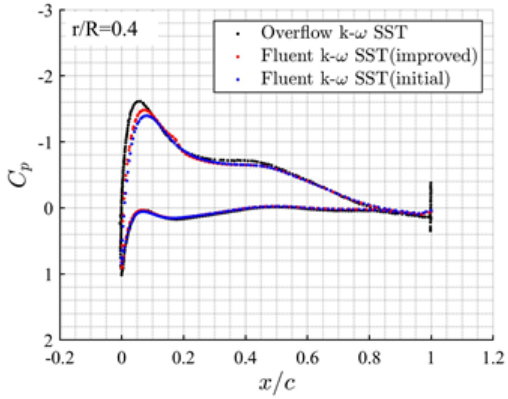
r/R=0.4
Overflow k-ω SST
Fluent k-ω SST(improved)
Fluent k-ω SST(initial)
C_p
x/c

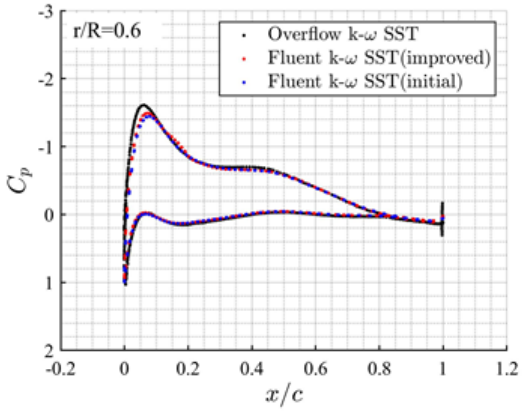
r/R=0.6
Overflow k-ω SST
Fluent k-ω SST(improved)
Fluent k-ω SST(initial)
C_p
x/c

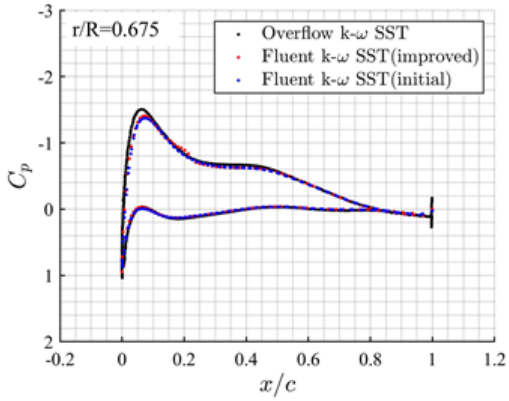
r/R=0.675
Overflow k-ω SST
Fluent k-ω SST(improved)
Fluent k-ω SST(initial)
C_p
x/c

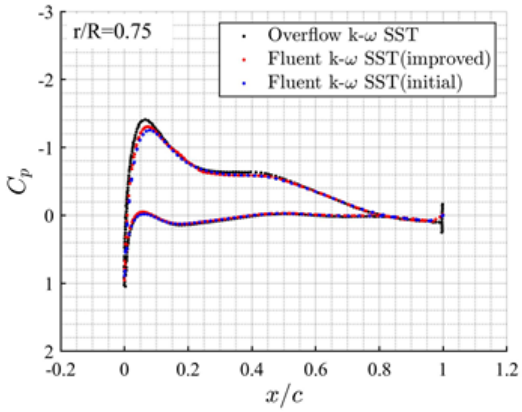
r/R=0.75
Overflow k-ω SST
Fluent k-ω SST(improved)
Fluent k-ω SST(initial)
C_p
x/c

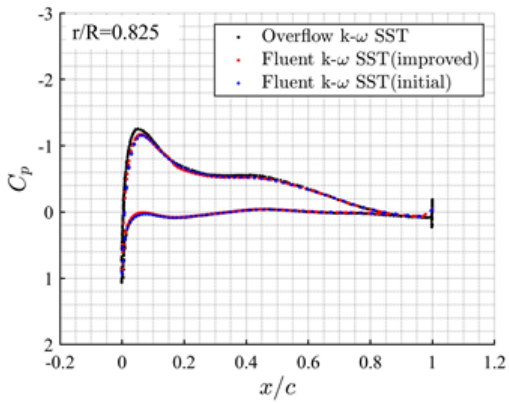
r/R=0.825
Overflow k-ω SST
Fluent k-ω SST(improved)
Fluent k-ω SST(initial)
C_p
x/c

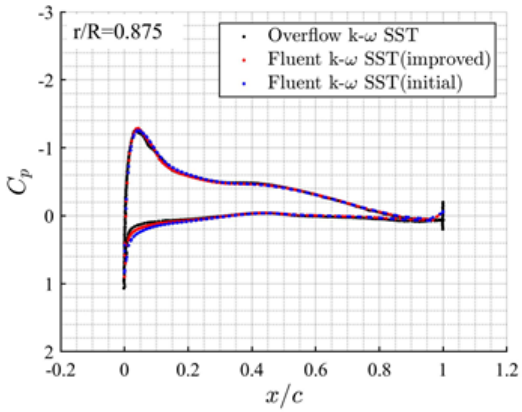
r/R=0.875
Overflow k-ω SST
Fluent k-ω SST(improved)
Fluent k-ω SST(initial)
C_p
x/c

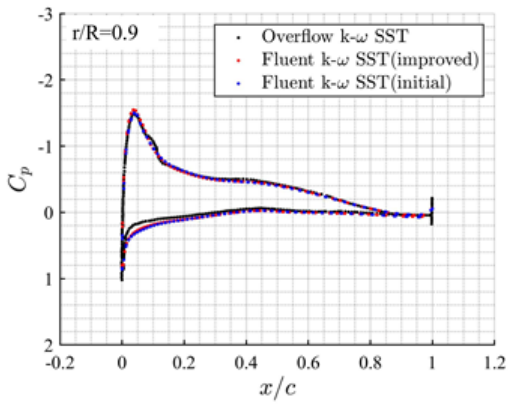
r/R=0.9
Overflow k-ω SST
Fluent k-ω SST(improved)
Fluent k-ω SST(initial)
C_p
x/c

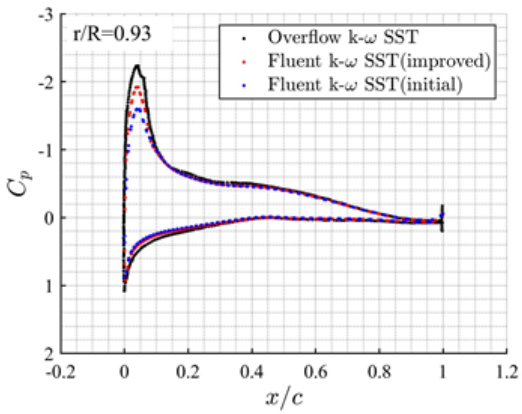
r/R=0.93
Overflow k-ω SST
Fluent k-ω SST(improved)
Fluent k-ω SST(initial)
C_p
x/c

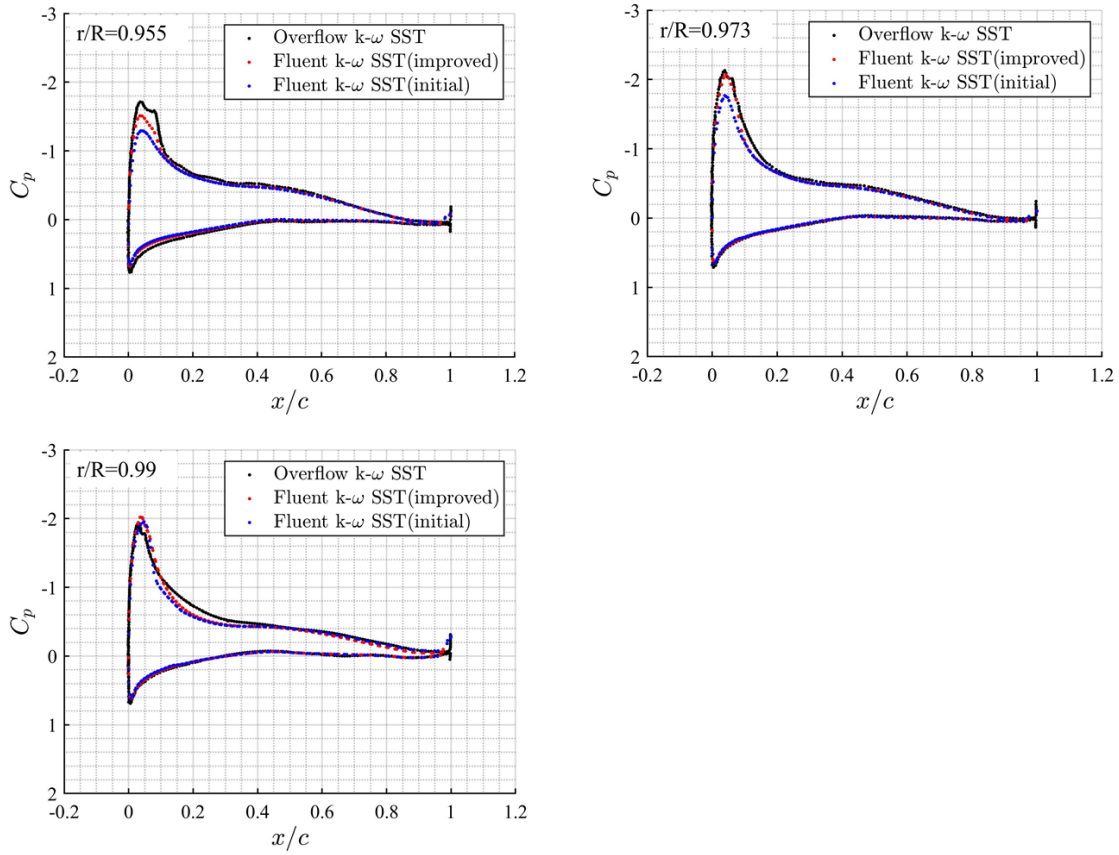

Figure A.2: Surface pressure distribution plots at 10° pitch setting (first comparison).

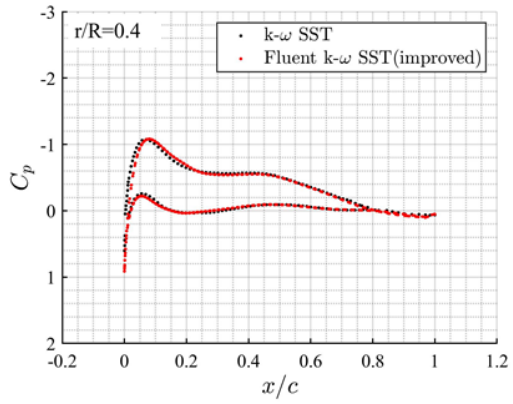
r/R=0.4
k-ω SST
Fluent k-ω SST(improved)
C_p
x/c

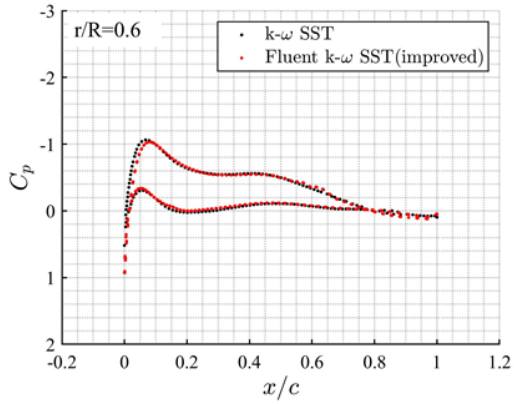
r/R=0.6
k-ω SST
Fluent k-ω SST(improved)
C_p
x/c

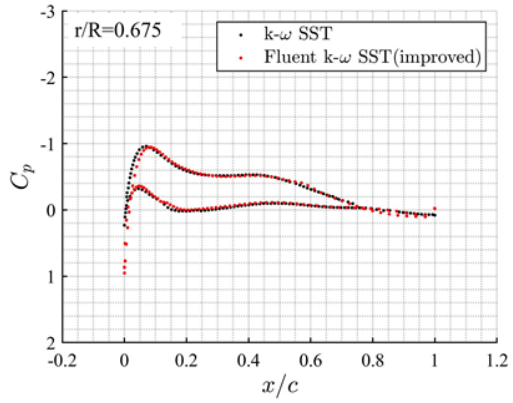
r/R=0.675
k-ω SST
Fluent k-ω SST(improved)
C_p
x/c

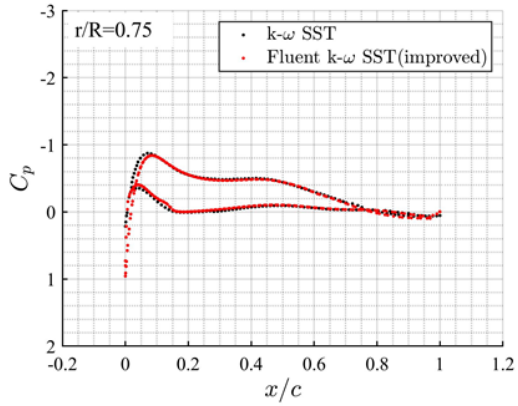
r/R=0.75
k-ω SST
Fluent k-ω SST(improved)
C_p
x/c

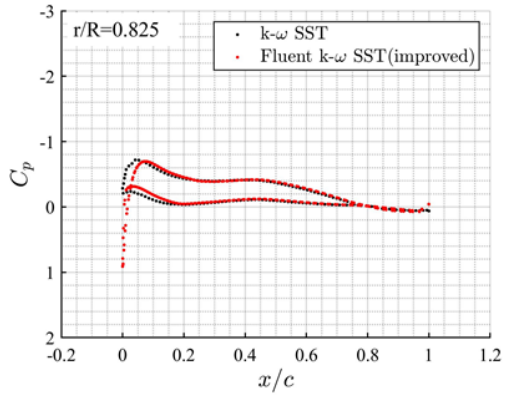
r/R=0.825
k-ω SST
Fluent k-ω SST(improved)
C_p
x/c

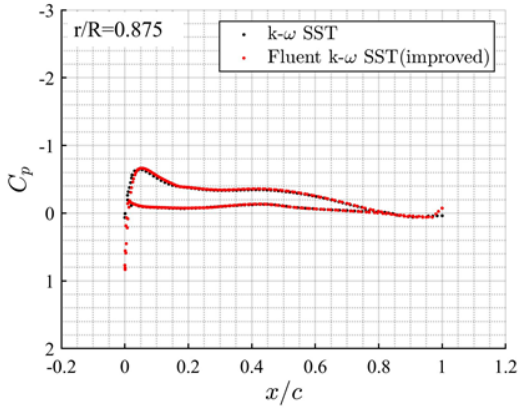
r/R=0.875
k-ω SST
Fluent k-ω SST(improved)
C_p
x/c

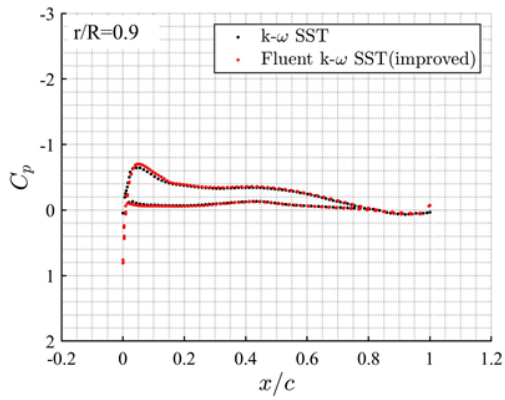
r/R=0.9
k-ω SST
Fluent k-ω SST(improved)
C_p
x/c

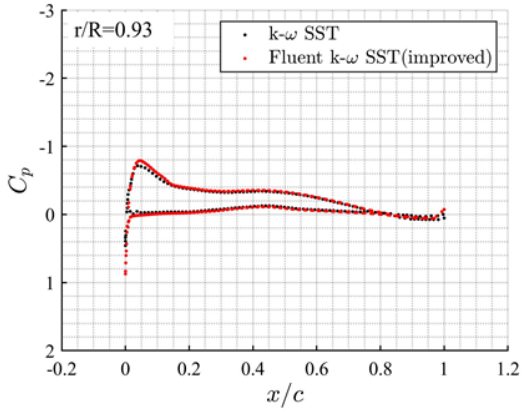
r/R=0.93
k-ω SST
Fluent k-ω SST(improved)
C_p
x/c

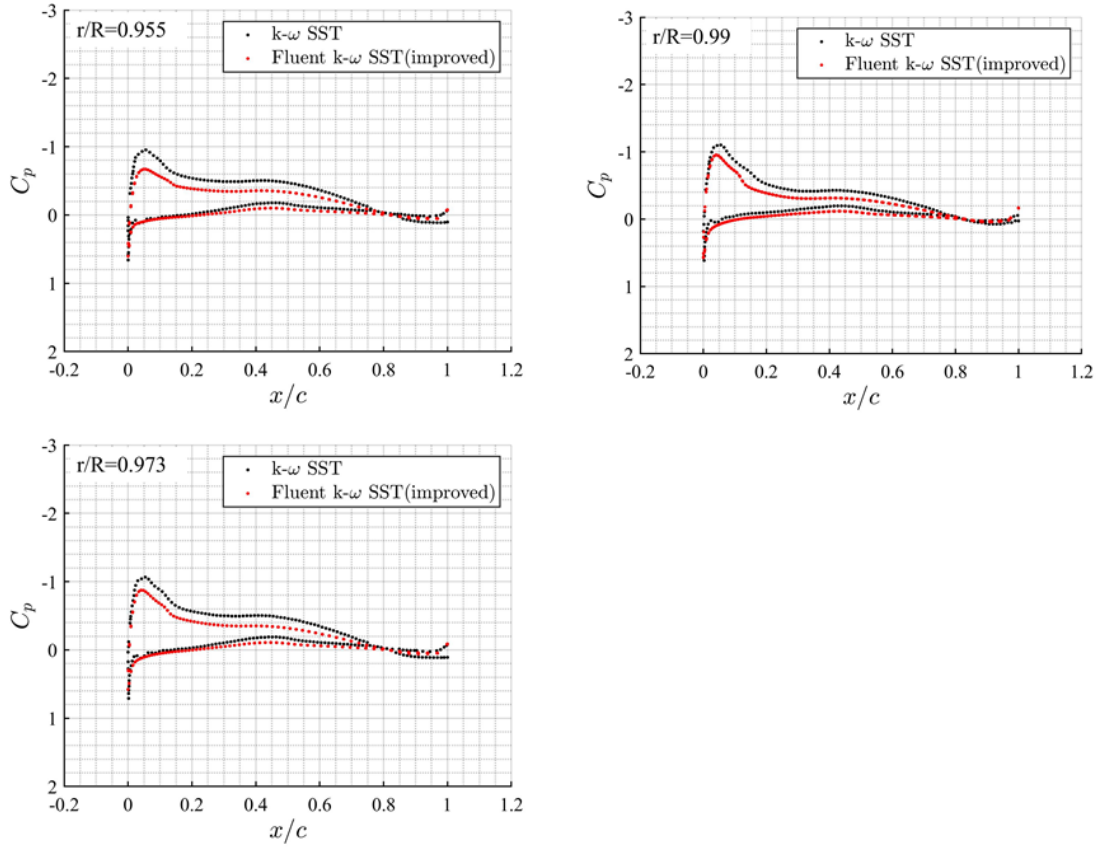

Figure A.3: Surface pressure distribution plots at 6° pitch setting (second comparison).

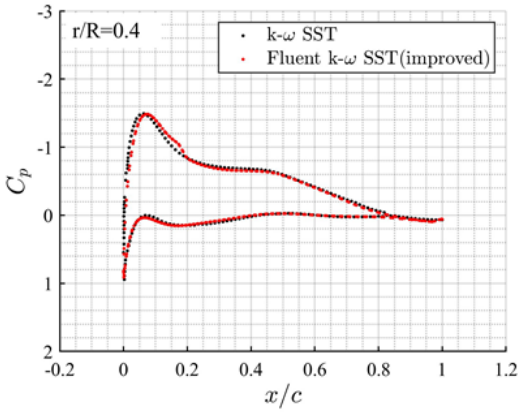
r/R=0.4
k-ω SST
Fluent k-ω SST(improved)
C_p
x/c

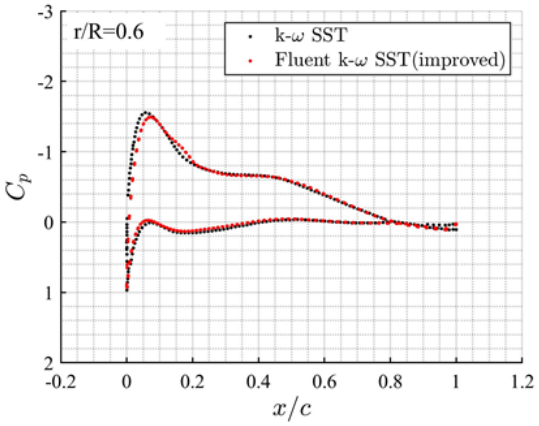
r/R=0.6
k-ω SST
Fluent k-ω SST(improved)
C_p
x/c

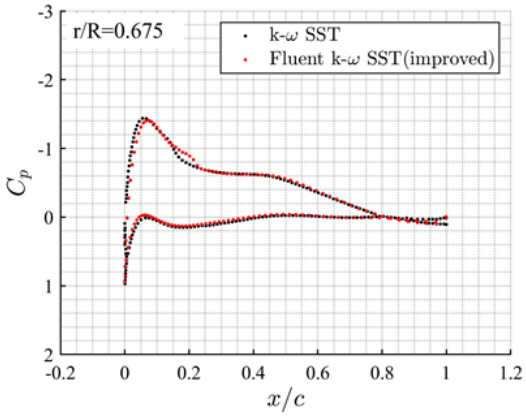
r/R=0.675
k-ω SST
Fluent k-ω SST(improved)
C_p
x/c

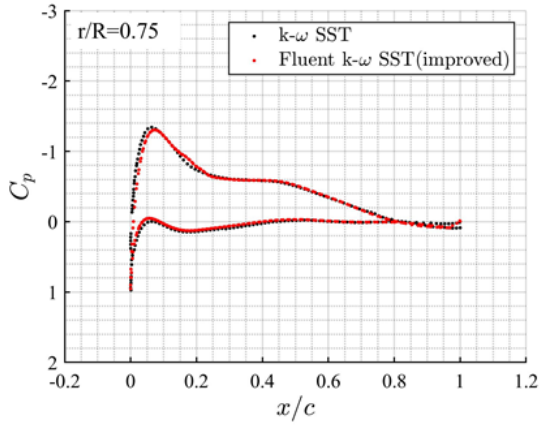
r/R=0.75
k-ω SST
Fluent k-ω SST(improved)
C_p
x/c

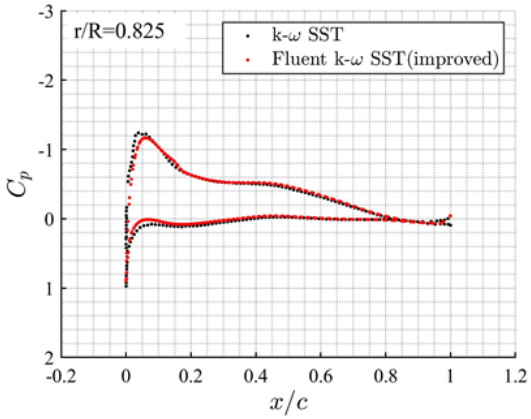
r/R=0.825
k-ω SST
Fluent k-ω SST(improved)
C_p
x/c

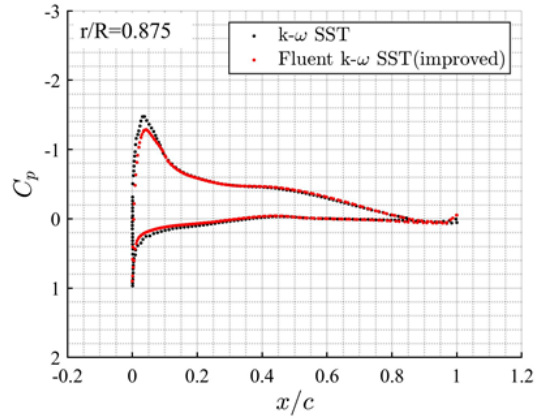
r/R=0.875
k-ω SST
Fluent k-ω SST(improved)
C_p
x/c

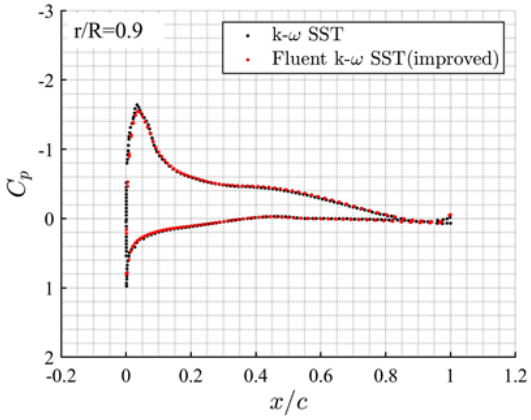
r/R=0.9
k-ω SST
Fluent k-ω SST(improved)
C_p
x/c

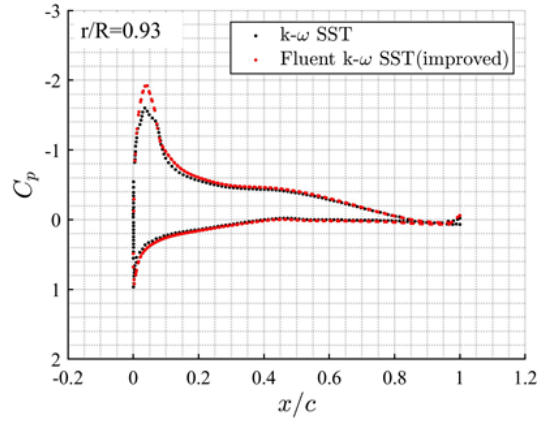
r/R=0.93
k-ω SST
Fluent k-ω SST(improved)
C_p
x/c

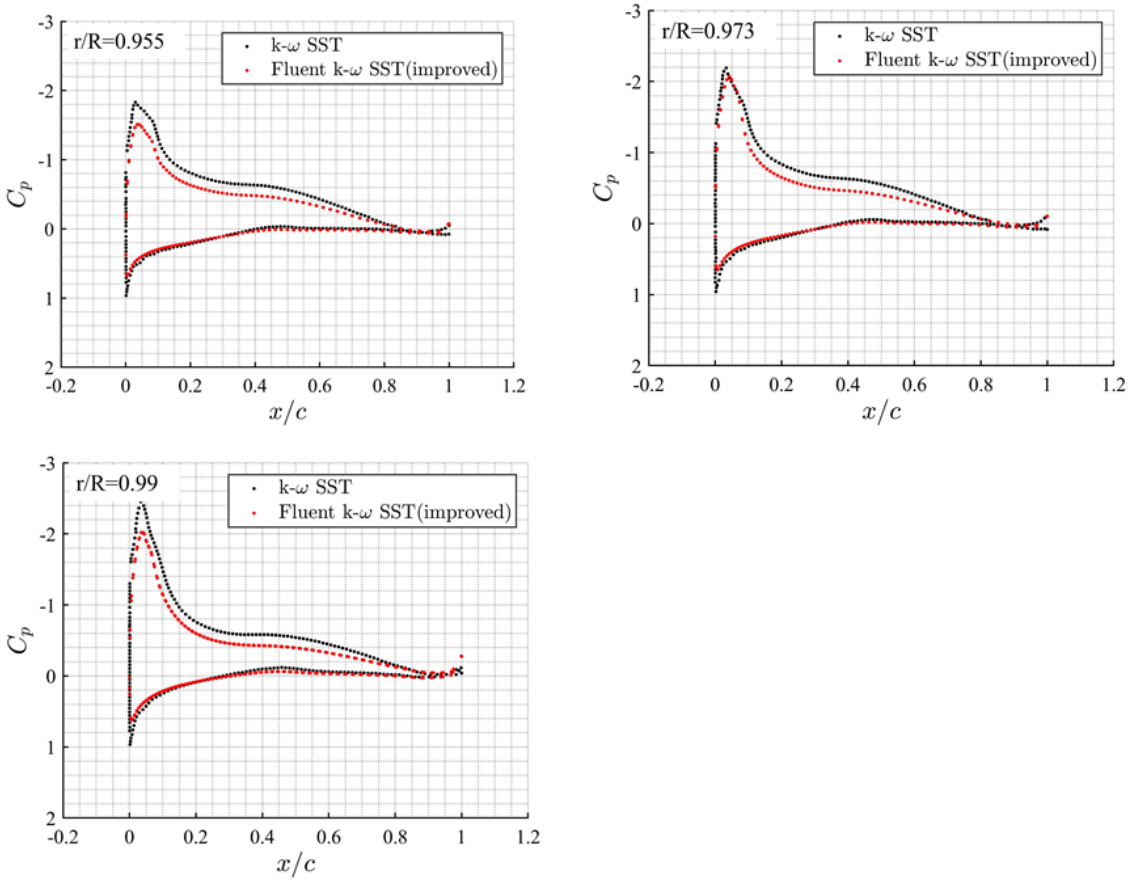

Figure A.4: Surface pressure distribution plots at 10° pitch setting (second comparison).

REFERENCES

[1] H. Mali, K. Benmansour, P.-W. Chen, and L. N. Sankar, "Aerodynamic simulations of the HVAB rotor in hover," in *AIAA SCITECH 2022 Forum*, San Diego, CA & Virtual: American Institute of Aeronautics and Astronautics, Jan. 3, 2022, ISBN: 978-1-62410-631-6.

[2] R. P. Narducci, R. Jain, J. Abras, and N. S. Hariharan, "HVAB rotor hover computational prediction: A comparative study using OVERFLOW and HPCMP CREATE™-AV helios," in *AIAA Scitech 2021 Forum*, VIRTUAL EVENT: American Institute of Aeronautics and Astronautics, Jan. 11, 2021, ISBN: 978-1-62410-609-5.

[3] F. R. Menter, "Two-equation eddy-viscosity turbulence models for engineering applications," *AIAA Journal*, vol. 32, no. 8, pp. 1598–1605, Aug. 1994.

[4] T. R. Norman, "AIAA APATC rotorcraft discussion group meeting," Presentation, Presentation, NASA Ames Research Center, Jan. 13, 2021.

[5] R. Jain, "CFD hover performance and transition predictions on the PSP and HVAB rotors using CREATE ^{TM} -AV helios," in *AIAA SCITECH 2022 Forum*, San Diego, CA & Virtual: American Institute of Aeronautics and Astronautics, Jan. 3, 2022, ISBN: 978-1-62410-631-6.

[6] S. H. Park, J. Han, and O. J. Kwon, "Numerical study of HVAB rotor using a mixed mesh flow solver," in *AIAA Scitech 2021 Forum*, VIRTUAL EVENT: American Institute of Aeronautics and Astronautics, Jan. 11, 2021, ISBN: 978-1-62410-609-5.

[7] S. H. Park and O. J. Kwon, "Numerical simulation of HVAB rotor in hover using a mixed-mesh flow solver," *Journal of Mechanical Science and Technology*, vol. 36, no. 6, pp. 2969–2979, Jun. 2022.

[8] P. Doerffer and O. Szulc, "Numerical simulation of model helicopter rotor in hover," *TASK QUARTERLY*, vol. 12, pp. 227–236, Sep. 2008.

[9] Q. Zhao and C. Sheng, "Predictions of HVAB rotor in hover using hybrid RANS/LES methods - II," in *AIAA SCITECH 2022 Forum*, San Diego, CA & Virtual: American Institute of Aeronautics and Astronautics, Jan. 3, 2022, ISBN: 978-1-62410-631-6.

[10] B. Lee, Y. S. Jung, D. Jude, and J. D. Baeder, "Turbulent transition prediction of PSP hovering rotor using -re $_t$ -SA with crossflow transition model," in *AIAA Scitech 2019 Forum*, San Diego, California: American Institute of Aeronautics and Astronautics, Jan. 7, 2019, ISBN: 978-1-62410-578-4.

[11] B. Lee and J. D. Baeder, "The effect of time marching on the wake structure breakdown in a hovering rotor simulation," in *AIAA Scitech 2021 Forum*, VIRTUAL EVENT: American Institute of Aeronautics and Astronautics, Jan. 11, 2021, ISBN: 978-1-62410-609-5.

[12] J. Abras and N. S. Hariharan, "Investigation of the impact of deep convergence on numerical wake breakdown of hovering rotors," in *AIAA Scitech 2021 Forum*, VIRTUAL EVENT: American Institute of Aeronautics and Astronautics, Jan. 11, 2021, ISBN: 978-1-62410-609-5.

[13] N. S. Hariharan, R. P. Narducci, E. Reed, and A. Egolf, "AIAA standardized hover simulation: Hover performance prediction status and outstanding issues," in *55th AIAA Aerospace Sciences Meeting*, Grapevine, Texas: American Institute of Aeronautics and Astronautics, Jan. 9, 2017, ISBN: 978-1-62410-447-3.

[14] S. H. Park and O. J. Kwon, "Numerical study of isolated and full configuration PSP rotor using a mixed mesh flow solver," in *AIAA Scitech 2020 Forum*, Orlando, FL: American Institute of Aeronautics and Astronautics, Jan. 6, 2020, ISBN: 978-1-62410-595-1.

[15] M. K. Jung, J. Y. Hwang, and O. J. Kwon, "Assessment of rotor aerodynamic performances in hover using an unstructured mixed mesh method," in *52nd Aerospace Sciences Meeting*, National Harbor, Maryland: American Institute of Aeronautics and Astronautics, Jan. 13, 2014, ISBN: 978-1-62410-256-1.

[16] R. P. Marpu, L. N. Sankar, S. M. Makinen, T. A. Egolf, J. D. Baeder, and M. Wasikowski, "Physics-based modeling of maneuver loads for rotor and hub design," *Journal of Aircraft*, vol. 51, no. 2, pp. 377–389, Mar. 2014.

[17] Q. Zhao, J. Wang, and C. Sheng, "Numerical simulations and comparisons of PSP and s-76 rotors in hover," in *2018 AIAA Aerospace Sciences Meeting*, Kissimmee, Florida: American Institute of Aeronautics and Astronautics, Jan. 8, 2018, ISBN: 978-1-62410-524-1.

[18] J. Carnes and J. G. Coder, "Computational assessment of the HVAB rotor in hover using laminar-turbulent transition modeling," in *AIAA Scitech 2019 Forum*, San Diego, California: American Institute of Aeronautics and Astronautics, Jan. 7, 2019, ISBN: 978-1-62410-578-4.

[19] N. A. R. Nik Mohd and G. Barakos, "Performance and wake analysis of rotors in axial flight using computational fluid dynamics," *Journal of Aerospace Technology and Management*, vol. 9, no. 2, pp. 193–202, Apr. 24, 2017.